Embedding a One-column Ocean Model (SIT 1.06) in the Community Atmosphere Model 5.3 (CAM5.3; CAM5–SIT v1.0) to Improve Madden–Julian Oscillation Simulation in Boreal Winter

Yung-Yao Lan, Huang-Hsiung Hsu*, Wan-Ling Tseng, and Li-Chiang Jiang

Research Center for Environmental Changes, Academia Sinica, Taipei 11529, Taiwan

*Correspondence to: Huang-Hsiung Hsu (hhhsu@gate.sinica.edu.tw)

Abstract

The effect of the air–sea interaction on the Madden–Julian Oscillation (MJO) was investigated using the one-column ocean model Snow–Ice–Thermocline (SIT 1.06) embedded in the Community Atmosphere Model 5.3 (CAM5.3; hereafter CAM5–SIT v1.0). The SIT model with 41 vertical layers was developed to simulate sea surface temperature (SST) and upper-ocean temperature variations with a high vertical resolution that resolves the cool skin and diurnal warm layer and the upper oceanic temperature gradient. A series of 30-year sensitivity experiments were conducted in which various model configurations (e.g., coupled versus uncoupled, vertical resolution and depth of the SIT model, coupling domains, and absence of the diurnal cycle) were considered to evaluate the effect of air–sea coupling on MJO simulation. Most of the CAM5–SIT experiments exhibit higher fidelity than the CAM5-alone experiment in characterizing the basic features of the MJO such as spatiotemporal variability and the eastward propagation in boreal winter. The overall MJO simulation performance of CAM5–SIT benefits from (1) better resolving the fine vertical structure of upper-ocean temperature and therefore the air–sea interaction that result in more realistic intraseasonal variability in both SST and atmospheric circulation and (2) the adequate thickness of a vertically-gridded ocean layer. The sensitivity experiments demonstrate the necessity of coupling the tropical eastern Pacific in addition to the tropical Indian Ocean and the tropical western Pacific. Coupling is more essential in the south than north of the equator in the tropical western Pacific. Enhanced MJO could be obtained without considering the diurnal cycle in coupling.

1. Introduction

The Madden–Julian Oscillation (MJO) is a tropical large-scale convection circulation system that propagates eastward across the warm pool region from the tropical Indian Ocean (IO) to the western Pacific (WP) on an intraseasonal time scale (Madden and Julian, 1972). The MJO is not just an atmospheric phenomenon. The findings from a multi-nation field campaign in the tropics called the Dynamics of MJO/Cooperative Indian Ocean Experiment on Intraseasonal Variability in the Year 2011 (DYNAMO/CINDY2011; de Szoeke et al., 2017; Johnson and Ciesielski, 2017; Pujiana et al., 2018; Yoneyama et al., 2013; Zhang and Yoneyama, 2017) revealed vigorous air–sea coupling during the evolution of the MJO (Chang et al., 2019; DeMott et al., 2015; Jiang et al., 2015, 2020; Kim et al., 2010; Li et al., 2016; Li et al., 2020; Newman et al., 2009; Pei et al., 2018; Tseng et al., 2014). During the suppression of convection, the MJO propagates eastward with light winds, which is accompanied by enhanced downwelling shortwave radiation absorption, weaker upward latent and sensible fluxes, less cloudiness and precipitation, and weaker vertically turbulent mixing in the upper ocean, thus causing an increase in the upper-ocean temperature. In the following active phase when deep convection occurs, downwelling shortwave radiation is reduced and stronger westerly winds enhance latent/sensible heat flux (LHF/SHF) loss from the ocean surface, thus causing a decrease in the upper-ocean temperature (DeMott et al., 2015; Madden and Julian, 1972, 1994; Zhang, 2005).

In addition to the tropical ocean surface, the structure of the upper ocean also evolves. Alappattu et al. (2017) reported that during an MJO event, surface flux perturbations cause changes in the ocean thermohaline structure, thus affecting the mixed-layer temperature. The following change in sea surface temperature (SST) can further affect atmospheric circulation of the MJO. Variations in SST mediate LHF and

SHF exchange across the air–sea interface. Although SST responds to atmospheric forcing, the modulation of LHF and SHF provides feedback to the atmosphere (DeMott et al., 2015; Jiang et al., 2020). Li et al. (2008, 2020) proposed that the phase relationship between SST and convection implies a delayed air–sea interaction mechanism whereby a preceding active-phase MJO may trigger an inactive-phase MJO through the delayed effect of the induced SST anomaly over the IO. The reduction in SST caused by a preceding active-phase MJO may, in turn, yield delayed ocean feedback that initiates a suppressed-phase MJO, and vice versa. The by-no-means negligible effect of intraseasonal SST variations caused by surface heat fluxes suggests that the ocean state can affect the MJO (DeMott et al., 2015, 2019; Hong et al., 2017; Li et al., 2020).

Since its discovery almost five decades ago, the MJO remains a phenomenon that poses a challenge to the capacity of state-of-the-art atmospheric general circulation models (AGCMs) such as those participating in the Coupled Model Intercomparison Project phase 5 and 6 to generate successful simulations (Ahn et al., 2017, 2020; Bui and Maloney 2018; Jiang et al., 2020; Hung et al., 2013; Kim et al., 2011).

Recent studies have reported that air–sea coupling improves the representation of the MJO in numerical simulation (Bernie et al., 2008; Crueger et al., 2013; DeMott et al., 2015; Li et al., 2016; Li et al., 2020; Tseng et al., 2014; Woolnough et al., 2007). Tseng et al. (2014) indicated that effectively resolving the tropical upper-ocean warm layer to capture temperature variations in the upper few meters of the ocean could improve MJO simulation. DeMott et al. (2015) suggested that the tropical atmosphere–ocean interaction may sustain or amplify the pattern of the enhanced and suppressed atmospheric convection of the eastward propagation. DeMott et al. (2019) demonstrated that the improved MJO eastward propagation in four coupled models

resulted from enhanced low-level convective moistening for a rainfall rate of >5 mm day^{-1} due to air–sea coupling. In addition, numerical experiments have been performed to investigate the effect of the diurnal cycle on the MJO (Hagos et al., 2016; Oh et al., 2013), with the results suggesting that the strength and propagation of the MJO through the Maritime Continent (MC) were enhanced when the diurnal cycle was ignored.

Although previous studies have demonstrated the importance of considering the air–sea interaction in a numerical model to improve MJO simulation, additional details regarding model configuration (e.g., vertical resolution and total depth of the vertically-gridded ocean, coupling domain, and absence of the diurnal cycle in air–sea coupling) have not been systematically explored. Tseng et al. (2014) coupled the one-column ocean model Snow–Ice–Thermocline (SIT; Tu and Tsuang, 2005) to the fifth generation of the ECHAM AGCM (ECHAM5–SIT) in the tropics and indicated that a vertical resolution of 1 m was essential to yield an improved simulation of the MJO with a realistic strength and eastward propagation speed.

In this study, we coupled the SIT model to the Community Atmosphere Model version 5.3 (CAM5.3; Neale et al., 2012)—the atmosphere component of the Community Earth System Model version 1.2.2 (CESM1.2.2; Hurrell et al., 2013) —to explore the improvement of MJO simulation by coupling SIT model to another AGCM is reproducible in modeling science. The CAM5.3, which has been widely used for the long-term simulation of the climate system, could not efficiently simulate the eastward propagation of the MJO; instead, the model simulated a tendency for the MJO to move westward in the IO (Boyle et al., 2015, Jiang et al, 2015). By contrast, the updated CESM2 with the new CAM6 could realistically simulate the MJO (Ahn et al., 2020; Danabasoglu et al., 2020). Thus, the well-explored CAM5, which does not produce a realistic MJO, appears to be a favorable choice for exploring coupling a

simple one-dimensional (1-D) ocean model over the tropical oceans, such as the SIT model, can improve MJO simulation, as well as the effects of model configuration on the degree of the improvement. Such a study can also enhance our understanding regarding the effect of air–sea coupling on the MJO.

The MJO is a tropical atmosphere system that exhibits a more substantial eastward propagation in boreal winter than in other seasons was the targeted feature in this study. To examine the sensitivity of MJO simulations to different configurations of the tropical air–sea coupling, we conducted a series of 30-year numerical experiments by considering various model configurations (e.g., coupled versus uncoupled, vertical resolution and depth of the SIT model, coupling domains, and absence of the diurnal cycle) to investigate the effect of air–sea coupling. This paper is organized as follows. Section 2 describes the data for validation, the model used for simulation, and the design of numerical experiments. Section 3 describes the effect of various tropical air–sea coupling configurations on the MJO simulation determined through detailed MJO diagnostics. Discussion and conclusions are provided in Section 4.

2. Data, methodology, model description, and experimental designs

2.1 Data and methodology

The data analyzed in this study include precipitation from the Global Precipitation Climatology Project (GPCP), outgoing longwave radiation (OLR) and daily SST (Optimum Interpolation SST; OISST) from the National Oceanic and Atmosphere Administration (NOAA), and parameters from the ERA-Interim (ERA-I) reanalysis (Adler et al., 2003; Dee et al., 2011; Lee et al., 2011; Reynolds and Smith, 1995; Schreck et al., 2018). The SST data for the SIT model were obtained from the Hadley Centre Sea Ice and Sea Surface Temperature dataset (Rayner et al., 2003;

HadISST1) and the ocean subsurface data (40-layer climatological ocean temperature, salinity, and currents) for nudging were retrieved from the National Centers for Environmental Prediction (NCEP) Global Ocean Data Assimilation System (GODAS; Behringer and Xue, 2004).

We used the CLIVAR MJO Working Group diagnostics package (CLIVAR, 2009) and a 20–100-day filter (Kaylor, 1977; Wang et al., 2014) to determine intraseasonal variability. MJO phases were defined following the index (namely, RMM1 and RMM2) proposed by Wheeler and Hendon (2004), which considered the first two principal components of the combined near-equatorial OLR and zonal winds at 850 and 200 hPa. The band-passed filtered data were used for calculating the index and defining phases.

2.2 Model description

2.2.1 CAM5.3

The CAM5.3 used in this study has a horizontal resolution of 1.9° latitude × 2.5° longitude and 30 vertical levels with the model top at 0.1 hPa. The MJO could not be realistically simulated in the CAM5.3. Boyle et al. (2015) demonstrated that although making the deep convection dependent on SST improved the simulation of the MJO variance, it exerted a significant negative effect on the mean-state climate of low-level cloud and absorbed shortwave radiation. By comparing the simulation results of an uncoupled and coupled CAM5.3, Li et al. (2016) suggested that air–sea coupling and the convection scheme most significantly affected the MJO simulation in the climate model.

2.2.2 1-D high-resolution TKE ocean model

The 1-D high-resolution turbulence kinetic energy (TKE) ocean model SIT was

used to simulate the diurnal fluctuation of SST and surface energy fluxes (Lan et al., 2010; Tseng et al., 2014; Tu and Tsuang, 2005). A description of the 1-D high-resolution ocean model SIT can be found in the appendix. The model was well verified against in situ measurements on board the R/V Oceanographic Research Vessel 1 and 3 over the South China Sea (Lan et al., 2010) and on R/V Vickers over the tropical WP (Tu and Tsuang, 2005).

The SIT model determines the vertical profiles of the temperature and momentum of a water column from the surface down to the seabed, except in the fixed ocean model bottom experiment. The default setting of vertical discretization (e.g., in the control coupled experiment) is 41 layers with 12 layers in the first 10.5 m, 6 layers between 10.5 m and 107.8 m (appendix Fig. A1). In the 1-D TKE ocean model, temperature and salinity below 107.8 m, where vertical turbulent mixing is greatly weakened, are nudged toward the climatological values of GODAS data until 4607 m. The extra high vertical resolution is needed to catch detailed temporal variation of upper ocean temperature characterized by the warm layer and cool skin (Tu and Tsuang, 2005). To account for the neglected horizontal advection heat flux, the ocean is weakly nudged (by using a 30-day time scale) between 10.5 m and 107.8 m and strongly nudged (by using a 1-day time scale) below 107.8 m according to the NCEP GODAS climatological ocean temperature. No nudging is performed within the upper-most 10.5 m. The SIT model calculates twice for each CAM5 time step (30 min; i.e., coupling 48 times per day).

2.3 Experimental design

A series of 30-year numerical experiments (Table 1) were conducted to investigate the effect of the air–sea interaction on the MJO simulation. The HadSST1 used to force the coupled and uncoupled model was the climatological monthly-mean

SST averaged over 1982-2001. The monthly SST was linearly interpolated to daily SST fluctuation that forced the model. The SST in the air–sea coupling tropical region was recalculated by the SIT during the simulation, while the prescribed annual cycle of SST was used in the areas outside the coupling region. Ocean bathymetry of the SIT was derived from the NOAA ETOPO1 data (Amante and Eakins, 2009) and interpolated into 1.9° × 2.5° horizontal resolution.

All simulations were driven by the prescribed annual cycle of SST repeatedly for 30 years. The strategy is to evaluate the simulation capacity of climate models under the same condition without considering interannual variation induced by SST. This approach has been widely adopted in many studies (Delworth et al., 2006; Haertel et al., 2020; Subramanian et al., 2011; Tseng et al., 2014; Wang et al., 2005).

Atmospheric initial conditions and external forcing such as CO_2, ozone, and aerosol in near-equilibrium climate state around the year 2000 were taken from F_2000_CAM5 component set based on CESM1.2.2 framework development. The data has been commonly used in present-day simulations using CAM5 (e.g., He et al., 2017).

The setup of five sets of experiment conducted in this study are described as follows.

(1) A standalone CAM5.3 simulation forced by climatological monthly HadISST1 (A–CTL) and the control experiment of coupled CAM5–SIT simulation (C–30NS; 41 vertical levels, coupling in the entire tropics between 30°N and 30°S with a diurnal cycle). The reasons for tropical coupling are two folds. Considering that the MJO is essentially a tropical phenomenon, the coupling was implemented only between 30^{o}N and 30^{o}S. Secondly, coupling a one-dimensional ocean model in the extratropics without surface flux correction as in

our case would ignore the impacts of strong ocean currents (such as the Kuroshio and Gulf Stream) and result in large biases.

(2) Upper-ocean vertical resolution experiment: Two simulations with the first layer centering at 12 m (C–LR12m) and 34 m (C–LR34m). Further details of the experimental design are shown in appendix Fig. A1. This experiment is to demonstrate the significant improvement that a fine vertical resolution can achieve compared to the coarse resolution (e.g., tens of meters) that is often adopted in slab ocean model.

(3) Shallow ocean bottom experiment: Three simulations with the ocean model bottom at 10 m (C–HR1mB10m), 30 m (C–HR1mB30m), and 60 m (C–HR1mB60m) (appendix Fig. A2). Note that all experiments retained the same vertical resolution (e.g., 1 meter in the first top 10 meters of the ocean) but with various ocean bottom (i.e., 10, 30, and 60 meters). The purpose is to demonstrate how the total ocean heat content, which depends on the total depth of the ocean, can affect the MJO.

(4) Regional coupling experiment: Four simulations with the coupling region in 0°N–30°N (C–0_30N) and 0°S–30°S (C–0_30S) for latitudinal effect, and 30°E–180°E (C–30_180E) and 30°E–75°W (C–30E_75W) for longitudinal effect. The coupling domains are shown in Fig. 1. In this experiment we identified the key ocean basins where coupling is essential.

(5) Diurnal cycle experiment: To explore the effect of diurnal coupling cycle a non-diurnal simulation was conducted for a comparison with the C–30NS simulation. The non-diurnal simulation (C–30NS–nD) considers the air–sea interaction only once a day, namely, calculating SHF and LHF based on daily mean atmospheric variables and SST. To prevent the inconsistent local time in different regions, the coupling frequency at each grid point remained 48 times per day using the same

daily means of atmospheric variables and SST at that particular point. In contrast, the control simulation calculates air–sea fluxes 48 times a day based on instantons values. A comparison between the non-diurnal simulation and the control simulation reveals the effect of diurnal cycle in air–sea coupling.

3. Results and Discussion

The realistic simulation of the MJO has always been a major bottleneck in the development of climate models. In this section, we demonstrate the sensitivity of air–sea coupling experiments using a 1-D high-resolution ocean model significantly improves the MJO simulation by the CAM5.3. The period between November and April when the MJO is the most prominent was the targeted season in this study.

3.1 Improvement of MJO simulation through air–sea coupling

This subsection compares the MJO simulation of the control coupled experiment (C–30NS) with that of the uncoupled AGCM (A–CTL) forced by climatological monthly SST of HadISST1 to demonstrate the effect of air–sea coupling on the MJO simulation by coupling the SIT model to the CAM5.3 in the tropical belt (30°N–30°S).

3.1.1 Wavenumber–frequency spectra and eastward propagation characteristics

A wavenumber–frequency spectrum (W–FS) analysis was conducted to quantify propagation characteristics simulated in different experiments. The spectra of unfiltered U850 in ERA-I reanalysis, C–30NS, and A–CTL are shown in Fig. 2a–c, respectively. The C–30NS considering the coupling in 30ºN–30ºS realistically simulates eastward-propagating signals at zonal wavenumber 1 and 30–80-day periods (Fig. 2a–b), although with a slightly larger amplitude compared with ERA-I.

By contrast, the uncoupled A–CTL does not yield realistic simulation; instead, it simulates both eastward (wavenumber 1)- and westward (wavenumber 2)-propagating signals with an unrealistic spectral shift to time scales longer than 30–80-day.

The major features of the simulated MJO propagation were examined. Figure 2d–f show the time evolution of precipitation and U850 anomalies in Hovmöller diagrams, which represent lagged correlation coefficients between the precipitation averaged over 10°S–5°N, 75–100°E and the precipitation and U850 averaged over 10°N–10°S on intraseasonal timescales. Figure 2d indicates eastward propagation for both precipitation and U850 from the eastern IO to the dateline, with precipitation leading U850 by approximately a quarter of a cycle. The Hovmöller diagram derived from the C–30NS (Fig. 2e) exhibits the key characteristics of eastward propagation for both precipitation and U850 and the relative phases between the two, although the simulated correlation is slightly weaker than that derived from GPCP and ERA-I. By contrast, the uncoupled A–CTL simulates intraseasonal signals that propagate westward over the IO and weak and much slower eastward propagation crossing the MC and WP (Fig. 2f). The contrast between Fig. 2e and 2f demonstrate that coupling a 1-D TKE ocean model alone could lead to a significant improvement in an AGCM in simulating the major characteristics (e.g., amplitude, propagation direction and speed, and phase relationship between precipitation and circulation) of the MJO.

3.1.2 Coherence of the simulated MJO

Cross-spectral analysis was conducted to examine the coherence and phase lag between tropical circulation and convection, which were plotted over the tropical wave spectra. Figure 2g–i show the symmetric part (e.g., Wheeler and Kiladis, 1999) of OLR and U850 in ERA-I/NOAA data, C–30NS, and A–CTL, respectively. We present only the spectra between 0 to 0.35 day^{-1} to highlight the MJO and equatorial

Kelvin waves. The most prominent characteristics seen in ERA-I/NOAA data are the peak coherence at wavenumbers 1–3 and a phase lag of approximately 90° in the 30–80-day band (Ren et al., 2019; Wheeler and Kiladis 1999). The coupled experiment C–30NS simulates strong coherence in this low-frequency band (wavenumber 1) and exhibits a realistic phase lag relationship between U850 and OLR perturbations. However, the coherence at wavenumbers 2–3 for the 30–80-day period simulated by C–30NS is weaker than that in ERA-I/NOAA data. This undersimulation was also noted in CCSM4 (Subramanian et al., 2011), the uncoupled and coupled CAM4 and CAM5 (Li et al., 2016), and NorESM1-M (Bentsen et al., 2013), which had a version of the CAM as an AGCM. In summary, C–30NS considering the coupling between 30ºN–30ºS produces coherent and energetic patterns in the eastward-propagating intraseasonal fluctuations of U850 and OLR in the tropical IO and WP that are generally consistent with the MJO characteristics. By contrast, the MJO characteristics in A–CTL are considerably weaker than those in C–30NS and that in ERA-I/NOAA data.

3.1.3 Horizontal and vertical structures of the MJO across the MC

Figure 2j–o show the horizontal and vertical structures of the MJO when deep convection is the strongest over the MC (i.e., phase 5). Figure 2j–l present the 20–100-day filtered OLR (W m^{-2}, shaded) and 850-hPa wind (m s^{-1}, vector). C–30NS realistically simulated the enhanced tropical convection over the eastern IO and the Kelvin-wave-like easterly anomalies over the tropical WP despite undersimulating the convection over the MC (Fig. 2j and 2k). By contrast, A–CTL failed to simulate the enhanced convection over the eastern IO and MC; instead, it simulated considerably weaker convection and easterly winds over the MC and WP, respectively, than that in ERA-I/NOAA data (Fig. 2j and 2l).

Figure 2m–o show the vertical–longitudinal profiles of 20–100-day filtered 15°N–15°S averaged vertical velocity (OMEGA; Pa s^{-1}, shaded) and moist static energy tendency (dMSE/dt) anomalies (W m^{-2}, contour) at phase 5. The spatial distribution of negative OMEGA (ascending motion) anomalies generally agreed with OLR anomalies in C–30NS simulation and NOAA data over the Indo-Pacific region (Fig. 2m and 2n). The relatively spatial relationship between the ascending motion and dMSE/dt seen in ERA-I is well simulated in the coupled experiment C–30NS. For example, positive dMSE/dt anomalies on the eastern side of the anomalous ascent demonstrate that the energy recharge process occurs in advance of the MJO convection over the lower-tropospheric easterlies (Fig. 2m and 2n), whereas negative dMSE/dt anomalies on the western side reveal that the discharge process occurs during and after convection over the lower-tropospheric westerlies. By contrast, this phase relationship, considered to be an essential feature leading to the eastward propagation of an MJO (Hannah and Maloney 2014; Heath et al., 2021), is not properly simulated in the uncoupled experiment A–CTL (Fig. 2o), in which the simulated weak negative OMEGA is located between negative and positive dMSE/dt anomalies over weak lower-tropospheric wind anomalies and associated with weak convection over the MC (Fig. 2l).

The temporal evolution of NOAA OLR and ERA-I U850 (Fig. 3a) indicates that convection originating in the western IO is enhanced during its eastward propagation to the MC where it reaches the peak amplitude and then gradually weakened when continuing moving eastward to the dateline. In the coupled experiment C–30NS, this evolution of convectively coupled circulation is realistically simulated, although it is weaker than the strength seen in NOAA OLR (Fig. 3b). Moreover, the split of convection into two cells off the equator in phase 6 is appropriately simulated in C–30NS (P6 in Fig. 3a and 3b). This split was caused by

the topographic and land–sea contrast effects of the MC (Tseng et al., 2017). Associated with the split is the southward detouring of the anomalous convection during the passage of the MJO through the MC (Kim et al. 2017, Tseng et al., 2017; Wu and Hsu, 2009). After the passage of the MJO through the MC, the anomalous convection stays south of the equator and continues moving eastward to the dateline. In the uncoupled A–CTL, the systematic eastward propagation of convectively coupled MJO circulation from the IO into the MC is not simulated. Instead, the convection over the MC develops in situ at a later stage than that observed (e.g., P6 in Fig. 3c) and dissipated rapidly. The A–CTL simulates a pair of off-equator convection anomalies in the eastern IO during phase 2 (P2 in Fig. 3c) that moves westward toward the central IO and were amplified at later stages (e.g., P4 in Fig. 3c). This unrealistic evolution explains the westward propagation tendency observed in the Hovmöller diagram (Fig. 2f).

3.1.4 Characteristics of air–sea interaction

Figure 4a–c show the longitude–phase diagram in which the 20–100-day filtered precipitation (shaded) and SST (contour) anomalies were averaged over 10°S–10°N to determine the relationship between precipitation and SST fluctuations and to establish a link between air–sea coupling and convection. The propagation of the enhanced convection with positive SST anomalies to the east could be clearly seen in GPCP/OISST and the coupled experiment C–30NS (Fig. 4a and 4b). The highest SST anomaly (SSTA) leads the maximum precipitation anomaly by approximately 2–3 phases, and the SSTA begins to decrease following the onset of enhanced precipitation. The ERA-I and OISST data reveal the following relationship between net surface flux and SST: the decreased (increased) LHF/SHF and increased (decreased) downward radiation flux leading (lagging) the positive (negative) SSTA

east (west) of anomalous deep convection. This well-known lead–lag relationship reflecting the active air–sea interaction in an MJO is realistically simulated in the coupled experiment C–30NS (not shown).

The contrast between C–30NS and A–CTL confirms the key role of the air–sea interaction in contributing to the eastward propagation and demonstrates that the eastward propagation simulation can be markedly improved by incorporating the air–sea interaction process in the model, even when using a simple 1-D ocean model such as SIT.

3.1.5 Vertically tilting structure

The warm SST was the key forcing that contributed to the boundary layer convergence before the onset of deep convection (Li et al., 2020; Tseng et al., 2014). Hence, the warmer upper ocean enhances the low-level atmospheric convergence and then leads to enhanced low-level moisture and preconditioned deep convection and eastward propagation. This moistening process associated with warm ocean surface temperature is well simulated in the coupled experiment C–30NS but is not shown here. Instead, we present the coupling of moisture divergence (MD) and atmospheric circulation.

MD and zonal wind anomalies from the surface to the upper troposphere averaged over the 10°S–10°N and 120–150°E region are shown in Fig. 4d–f to depict the relationship between the vertically tilting structure of MD and zonal wind anomalies. Note that the active convection occurred around phase 5. The coupled experiment C–30NS (Fig. 4e) realistically simulates the deepening of coupled MD and zonal wind anomalies with time (Fig. 4d). An evolution from the right to left seen in each panel of Fig. 4d–f is equivalent to the eastward movement of vertically tilting circulation from the eastern IO into the MC because of the eastward-

propagating nature of the MJO. Figure 4d and 4e show that in both ERA-I reanalysis and the coupled experiment C–30NS, the near-surface convergence (negative MD) occurring in the easterly anomalies lead the convection and continued deepening up to 500 hPa from phase 2 to phase 6 when the easterly anomalies switch to westerly anomalies. By contrast, this evolution of coupled MD–zonal wind anomalies are not appropriately simulated in the uncoupled experiment (Fig. 4f). For example, a slow deepening with time is observed in the MD anomaly but not in the zonal wind anomaly that exhibits a vertically decayed structure, suggesting that MD and wind anomalies are not well coupled, as noted in the ERA-I/NOAA data and the control coupled experiment.

In the ERA-I reanalysis data, the negative near-surface MD anomalies appear first under the easterly anomaly and continue deepening between the easterly and westerly anomalies. This development in the phase relationship between MD and zonal wind anomalies in both ERA-I reanalysis data and the coupled simulation is consistent with the well-known structure embedded in the MJO, namely the near-surface convergence in the easterly phase (i.e., a boundary-layer moistening process; Kiranmayi and Maloney 2011; Li et al., 2020; Tseng et al., 2014), followed by the deep convection when transitioning to the westerly phase. This close phase relationship that is key to the eastward propagation is appropriately simulated in the coupled experiment but not in the uncoupled experiment.

3.1.6 Intraseasonal variance of precipitation

Figure 4g–i present the spatial distribution of intraseasonal variance of precipitation. In the GPCP data, the maximum variance is noted over the tropical eastern IO, MC, and tropical WP. The maximum variance south of the island in the MC and the equator in the tropical WP reflects the southward shift of the MJO deep

convection when passing through the MC, partly due to the blocking effect of mountainous islands and the higher moisture content over high SST south of the equator in the region during boreal winter (Kim et al., 2017; Ling et al., 2019; Sobel et al., 2008; Tseng et al., 2017; Wu and Hsu, 2009). Although the control coupled experiment fails to simulate the variance maximum in the tropical eastern IO, it appropriately simulates the maximum variance over the tropical WP, reflecting its ability to simulate the eastward propagation of the MJO through the MC. By contrast, the uncoupled A–CTL experiment simulates considerably weaker intraseasonal variance in both the tropical eastern IO and the tropical WP. Figure 4j–l are the 20–100-day filtered SST (K, shaded) and 850-hPa wind (m s^{-1}, vector) during MJO phase 7 when deep convection is the strongest over the dateline. The coupled experiment C–30NS realistically simulates the negative SST anomaly over the MC and WP when enhanced tropical convection passed through the MC to the dateline, indicating the capability of the SIT model to reproduce the SST anomaly by exchanging LHF/SHF between the atmosphere and ocean. In A-CTL, no SST anomaly is evident because the model was forced by prescribed climatological SST. The contrast seen in Fig. 4j–l demonstrates the essential role of atmosphere–ocean coupling in shaping the MJO. A delayed air–sea interaction mechanism was noted, where a preceding active-phase MJO may trigger an inactive-phase MJO through the delayed effect of the induced SST anomaly. In addition, the westerly winds at 850 hPa moving southward between MC and WP are captured by the control experiment C–30NS and are similar to the ERA-I reanalysis winds (Fig. 4j and 4k). By contrast, A–CTL forced by climatological monthly SST (<0.05 K $phase^{-1}$ anomaly) fails to simulate the southward westerly wind of the region extending from the MC to the dateline (Fig. 4l).

3.2 Effect of upper-ocean vertical resolution

In the control coupled experiment C–30NS, the vertical resolution in the upper 10.5 m was 1 m. Tseng et al. (2014) suggested that fine vertical resolution is crucial for appropriately simulating the eastward propagation. To investigate the effect of vertical resolution, two experiments with a thicker first layer were conducted by moving the center of the layer to 11.5 m (C–LR12m) and 33.9 m (C–LR34m), respectively, as opposed to the control experiment in which 10 layers were implemented in the first 10.5 meters (see appendix Fig. A1 for vertical discretization). The dramatic changes in vertical profile of ocean temperature between the fine and coarse resolution simulation are demonstrated in Fig.5, which presents the 20–100-day filtered oceanic temperature anomalies (K, shaded) between 0 and 60 m depth for MJO phase 1, 3, 5, and 7. The amplitude of ocean temperature is the largest in C–30NS and much weaker in C–LR12m and C–LR34m. In addition, there is a clear vertical stratification of ocean temperature in C–30NS, whereas C–LR12m and C–LR34m are well mixed because of not vertically gridded. This demonstrates the necessity of fine vertical gridding for resolving the quick fluctuation of ocean temperature when interacting with the atmosphere.

The W–FS spectral peaks of U850 in C–LR12m are concentrated in eastward-propagating wavenumber 1 at three timescales (e.g., longer than 80 days, 30–80 days, and approximately 30 days; Fig. 6a). In C–LR34m, both eastward and westward signals are simulated with the dominant W–FS timescale longer than 80 days (Fig. 6b). The appearance of both eastward and westward signals at a lower frequency implied a stronger stationary tendency or weaker eastward-propagating tendency. This result is consistent with that reported by Tseng et al. (2014) that the scientific reproducibility of coarser resolution causes a longer intraseasonal periodicity and slower eastward propagation of the MJO.

The effect of vertical resolution on the MJO simulation can be seen in the Hovmöller diagram. The eastward propagation simulated in C–LR12m (Fig. 6c) markedly weakened after crossing the MC compare with that simulated in the control experiment C–30NS (Fig. 2e). In C–LR34m, the quasi-stationary fluctuation and westward propagation are simulated over the IO (Fig. 6d), appearing similar to those in A–CTL (Fig. 2f). The lead–lag relationship between precipitation (zonal wind) and SST is poorly simulated in C–LR12m (Fig. 6e) and even more poorly simulated in C–LR34m (Fig. 6f). This result confirms the finding reported by Tseng et al. (2014) that a higher vertical resolution in the upper few meters below the surface allows for a faster air–sea interaction, thus resulting in a more realistic simulation of the MJO.

3.3 Effect of the lowest boundary of the SIT model

The ocean is a vital energy source for the MJO. Although vertical resolution is crucial for the efficiency of air–sea interaction, the thickness of the upper ocean that interacts with the atmosphere represents the ocean heat content to substantiate the MJO. A key question is how the total ocean heat content, which depends on the total depth of the ocean, can affect the MJO. Considering two models with the same vertical resolution, the model with thinner ocean (e.g., 10 meter) would interact as efficiently as another model with thicker ocean (e.g., 60m) but with much less heat to release to or to absorb from the atmosphere. The former would have less impact on the atmosphere than the latter. Using the same vertical resolution, three experiments with various ocean depths ocean bottom at 10, 30, and 60 m were conducted (see appendix Fig. A2 and Table 1).

The spectra and the Hovmöller diagrams shown in Fig. 7a–c and Fig. 7d–f, respectively, demonstrate that the thicker ocean model simulates a stronger MJO with a frequency closer to those in the coupled experiment C–30NS and ERA-I/NOAA

500 data, and more realistic eastward propagation. In addition, the lead–lag relationship
501 between precipitation (wind) and SST is more realistically simulated with increasing
502 thickness of the ocean model (Fig. 7g–i).
503 This result suggests that the thickness of the vertically-gridded ocean that interacts
504 with the atmosphere strongly affects the frequency of the simulated MJO. A thinner
505 (thicker) vertically-gridded ocean is more quickly (slowly) recharged and discharged
506 through SHF and LHF exchange between the atmosphere and ocean and therefore
507 likely fluctuates at a faster (slower) tempo. The simulated periodicity is therefore
508 affected by the thickness (or ocean heat content) of upper ocean that interacts
509 rigorously with the atmosphere. Although the result suggests 60 m is an appropriate
510 thickness to realistically simulate the periodicity of the MJO, we did not intend to
511 suggest the exact thickness required for a proper simulation because it might depend
512 on the model. The upper ocean should be adequately thick to contain a certain amount
513 of heat to generate appropriate periodicity. However, the reason for the intraseasonal
514 time scale (i.e., 20-100 days) should be determined in future studies. This finding
515 does not suggest a constant periodicity because periodicity might be affected by the
516 time-varying structure of the atmosphere and ocean in the real world.
517
518 **3.4 Effects of coupling domains**
519 The MJO is a planetary-scale phenomenon. Given its large-scale circulation, the
520 air–sea interaction affecting the MJO likely occurs in a much larger area than the
521 region near the major convection anomalies. In this section, we discuss the effect of
522 coupling domain on model ability to simulate the eastward propagation speed and
523 periodicity of the MJO. Four experiments considering the coupling in various
524 domains (C–0_30N, C–0_30S, C–30_180E, and C–30E_75W, Fig. 1) were conducted
525 for the purpose. The results are shown in Fig. 8. The C–0_30N that considered the

526 coupling in the tropics between the equator and 30°N simulates the least realistic MJO
527 propagation in terms of W–FS (Fig. 8a), zonal wind–precipitation coupling (Fig. 8e),
528 and SST–precipitation (Fig. 8i) among the four regional coupling experiments. By
529 contrast, coupling only the tropics between the equator and 30°S simulates a more
530 realistic MJO in all three aspects (i.e., spectrum in Fig. 8b, temporal evolution of
531 precipitation/wind, and precipitation/SST coupling in Fig. 8f and 8j). Figure. 9a
532 indicates that the negative OLR anomalies at phase 5 simulated in C–0_30N stays
533 mainly north of the equator and does not shift southward in the MC as revealed in
534 ERA-I reanalysis and NOAA OLR and in the control experiment C–30NS, and the
535 convection over the IO is unrealistically weak. By contrast, the southward detouring
536 in the MC is realistically simulated in C–0_30S that coupled only the tropical ocean
537 between the equator and 30°S. This result indicates that air–sea coupling occurring
538 south of the equator is the key to producing appropriate eastward propagation and
539 detouring of the MJO through the MC. Without this coupling, the C–0_30N
540 experiment fails to realistically simulate the eastward propagation of the MJO (Fig.
541 8e). This contrast can be attributed to the warmer ocean surface and higher moisture
542 content found south of the equator in boreal winter, which comprise a more favorable
543 environmental condition for air–sea coupling and convection–circulation coupling and
544 the occurrence of the MJO.

545 MJO simulations can be affected by air–sea coupling in the longitudinal domain.
546 Tseng et al. (2014) examined this effect by allowing coupling in different regions
547 (e.g., the IO, WP, and IO + WP) and found that the IO + WP coupling experiment
548 yielded the most satisfactory MJO simulation in terms of the zonal W–FS and
549 eastward propagation characteristics. In this study, we conducted sensitivity
550 experiments in which we allowed coupling in the tropics in two longitudinal domains,
551 namely 30°E–180°E (C–30_180E) and 30°E–75°W (C–30E_75W). The 30°E–180°E

552 region covered the IO and WP, and the 30°E–75°W region covered the IO and the
553 entire tropical Pacific. As shown in Fig. 8, the C–30E_75W experiment simulates
554 more realistic MJO than the C–30_180E experiment, with stronger eastward
555 propagation and larger amplitudes in the spectrum (Fig. 8c and 8d) and Hovmöller
556 diagrams of precipitation/wind (Fig. 8g and 8h) and precipitation/SST (Fig. 8k and
557 8l). The simulated MJO in C–30E_75W propagated farther east than that in C–
558 30_180E, particularly evident in Fig. 8k and 8l. The spatial distributions of circulation
559 and OLR shown in Fig. 9c and 9d indicate the presence of a stronger convective-
560 coupled circulation system over the MC and WP in C–30E_75W. These results
561 suggest that coupling over the entire tropical IO and Pacific could enhance the
562 strength and eastward propagation of the MJO and encourage farther propagation to
563 the central Pacific.
564
565 **3.5 Diurnal versus no diurnal cycle in air–sea coupling**
566 Previous studies showed that the diurnal cycle in the MC can weaken the MJO
567 and its eastward propagation (Hagos et al., 2016; Oh et al., 2013). We conducted an
568 experiment to determine whether computing surface heat fluxes using daily mean
569 values, instead of instantaneous values, of atmospheric variables and SST with the
570 same coupling frequency would affect the MJO simulation. The coupling in the model
571 was conducted through the SHF and LHF exchange between the atmosphere and
572 ocean, that were calculated based on simulated winds, moisture, and temperature. As
573 mentioned in Section 2.3, air–sea fluxes were calculated twice for every time step
574 (coupling 48 times per day) in the control coupled experiment (C–30NS) based on the
575 instantaneous values of atmospheric and oceanic variables. In the experiment in which
576 the diurnal cycle was removed (C–30NS–nD), air–sea fluxes were calculated as in C–
577 30NS but were based on daily means of both atmospheric variables and SST. Doing

this removed certain diurnal effects of air-sea coupling. The results shown in Fig. 10 reveal the enhancement of the eastward-propagating signals in the MJO (e.g., a larger amplitude in spectrum; Fig. 10a) and further eastward propagation (Fig. 10b) as well stronger coupling between precipitation and SST (Fig. 10c) in C–30NS–nD. The overall results are consistent with previous finding that the diurnal cycle tends to reduce the amplitude of the MJO, indicating that the weakening effect occurs through air–sea coupling in addition to those processes in the atmosphere. Previous studies have hypothesized that rapid interaction processes in the diurnal time scale tend to extract energy from the MJO, thus reducing the strength and propagation tendency of the MJO. However, a comparison between the spectra of C–30NS and C–30NS–nD indicates that the experiment in which the diurnal cycle is removed appeared to oversimulate the MJO with unrealistic strength, suggesting that the effect of the diurnal cycle should be considered in the model to simulate a more realistic MJO. However, whether this is a common result in different models remain to be examined.

4. Discussion and conclusions

Air–sea coupling is a key mechanism for the successful simulation of the MJO (Chang et al., 2019; DeMott et al., 2015; Jiang et al., 2015, 2020; Kim et al., 2010; Li et al., 2016; Li et al., 2020; Newman et al., 2009; Tseng et al., 2014). This study, following the study of Tseng et al. (2014), demonstrated that coupling a high-resolution 1-D TKE ocean model (namely the SIT model) to the CAM5, namely the CAM5–SIT, significantly improved the MJO simulation over the standalone CAM5. By coupling SIT model to an AGCM different from Tseng et al. (2014), this study confirms the scientific reproducibility for the improvement of MJO simulation in modeling science. The CAM5–SIT realistically simulates the MJO characteristics in many aspects (e.g., intraseasonal periodicity, eastward propagation, coherence in the

low-frequency band, detouring propagation across the MC, tilting vertical structure, and intraseasonal variance in the WP).

Systematic sensitivity experiments were conducted to investigate the effects of the vertical resolution and the thickness of the 1-D ocean model, coupling domains, and the absence of the diurnal cycle. The results of all the sensitivity experiments are summarized in Fig. 11a and 11b, which show four common metrics for MJO evaluation. The four metrics are the propagation speed of the MJO (estimated from the U850 Hovmöller diagram as Fig. 2d–f) versus the power ratio of eastward- and westward-propagating 30–80-day signals (E/W ratio, derived from the zonal W–FS) in Fig. 11a and the eastward propagation speed of the 30–80-day filtered precipitation anomaly (estimated from the precipitation Hovmöller diagram) versus the variance explained by RMM1 and RMM2 (i.e., the sum of the variance explained by the first two empirical orthogonal functions (EOF1 and EOF2) based on Wheeler and Hendon, 2004) in Fig. 11b. Based on the maximum precipitation anomaly and zero values of U850 (indicating deep convection region), propagation speeds of precipitation and U850 were calculated from Hovmöller diagrams between 60°E and 150°W. Overall, the control experiment C–30NS simulates the most realistic MJO among all sensitivity experiments.

As for vertical resolution, we determined that the MJO simulation efficiency decreased when the vertical resolution of the SIT model is decreased from 1 m to 11.5 or 33.9 m, as simulated in the C–LR12m and C–LR34m experiments, respectively. This finding, consistent with that reported by Tseng et al. (2014), suggests that a finer vertical resolution more effectively resolves temperature variations in the ocean warm layer and enhances atmospheric–ocean coupling, thus enabling the upper ocean to more efficiently respond to atmospheric forcing by providing sensible and latent heat fluxes; this results in superior synchronization between the lower atmosphere and the

upper ocean.

We observed that the shallower ocean model bottom could speed up the eastward propagation of the MJO by producing more perturbations of shorter periodicity (Fig. 7) and results in a weaker MJO. The shallower ocean layer with vertical grids likely responds more quickly to atmospheric forcing but provides less sensible and latent heat fluxes to the atmosphere. Thus, the MJO propagates too fast with a weaker amplitude.

In the coupling domain sensitivity experiments, we investigated the essential coupling domain required to simulate the realistic MJO and the effect of the domain on the MJO simulation. Coupling only the northern tropics fails to simulate the eastward propagation, whereas coupling only the southern tropics yields a more realistic MJO simulation, although this simulation is inferior to coupling the entire tropics. This contrast reveals the importance of the southern tropical ocean, especially in the MC where high SST and moisture content are noted. Coupling in the southern tropics is therefore essential for providing the energy required to maintain the MJO and its eastward propagation. By contrast, the northern tropics are relatively dry and cool. Coupling in this region is therefore less effective in improving MJO simulation.

In the longitudinal domain sensitivity experiments, we found that the MJO amplitude and the eastward extend of its eastward propagation are enhanced by extending the eastern boundary of the coupling domain from the tropical eastern IO to the tropical WP and further to the tropical eastern Pacific (Fig. 1). Further extension of the domain to cover the tropical Atlantic does not exhibit further enhancement (not shown). This result indicates that coupling in the tropical central and eastern Pacific, although not the major MJO signal regions (i.e., from the tropical IO to the tropical WP), still played a marked role in sustaining the MJO. We propose the following to explain this effect. Because of the planetary scale of the MJO, the near-surface

656 easterly circulation to the east of the convection core often extended to the tropical
657 central and eastern Pacific where the climatological easterly prevailed. The coupling
658 beyond the WP increased low-level moisture transport and convergence to the east of
659 the convection and establish an environment suitable for the further eastward
660 propagation of the MJO. This effect was likely terminated by the landmass of Central
661 America when the tropical Atlantic was further included. Thus, a further eastward
662 extension of the coupling domain exerted little effect on further enhancing the MJO. A
663 diagnostic study on the effect of the longitudinal coupling domain is being conducted,
664 and the results will be reported in a following paper.
665 The diurnal versus nondiurnal cycle experiment indicates that nondiurnal
666 coupling tended to enhance eastward-propagating signals but slow down the eastward
667 propagation (Fig. 11a–b). This result is consistent with the finding of previous studies
668 that the diurnal cycle in the atmosphere extracts energy from the MJO, thus
669 weakening it.
670 In this study, we demonstrated how air–sea coupling can improve the MJO
671 simulation in a GCM. The findings are as follows.
672 (1) Better resolving the fine structure of the upper-ocean temperature and therefore
673 the air–sea interaction leads to more realistic intraseasonal variability in both
674 tropical SST and atmospheric circulation.
675 (2) An adequate thickness of vertically-gridded upper ocean is required to simulate a
676 delayed response of the upper ocean to atmospheric forcing and lower-frequency
677 fluctuation.
678 (3) Coupling the tropical eastern Pacific, in addition to the tropical IO and the tropical
679 WP, can enhance the MJO and facilitate the further eastward propagation of the
680 MJO to the dateline.
681 (4) Coupling the southern tropical ocean, instead of the norther tropical ocean, is

essential for simulating a realistic MJO.

(5) Stronger MJO variability can be obtained without considering the diurnal cycle in coupling.

Our study confirmed the effectiveness of air–sea coupling for improving MJO simulation in a climate model and demonstrated how and where to couple. The findings enhance our understanding of the physical processes that shape the characteristics of the MJO.

Code and data availability. The model code of CAM5–SIT is available at https://doi.org/10.5281/zenodo.5510795. Input data of CAM5–SIT using the climatological Hadley Centre Sea Ice and Sea Surface Temperature dataset and GODAS data forcing, including 30-year numerical experiments, are available at https://doi.org/10.5281/zenodo.5510795.

Author contributions. HHH is the initiator and the primary investigator of the Taiwan Earth System Model project. YYL is the CAM5–SIT model developer and writes the majority part of the paper. WLT and LCJ assist in MJO analysis.

Competing interests. The authors declare that they have no conflict of interest.

Acknowledgements. The contribution from YYL, HHH, WLT, and LCJ to this study is supported by Ministry of Science and Technology of Taiwan under contracts MOST 110-2123-M-001-003, MOST 110-2811-M-001-603, MOST 109-2811-M-001-624 and MOST108-2811-M-001-643. Our deepest gratitude goes to the editors and anonymous reviewers for their careful work and thoughtful suggestions that have helped improve this paper substantially. We sincerely thank the National Center for

Atmospheric Research and their Atmosphere Model Working Group (AMWG) for release CESM1.2.2. We thank the computational support from National Center for High530 performance Computing of Taiwan. This manuscript was edited by Wallace Academic Editing.

Reference

Adler, R. F., Huffman, G. J., Chang, A., Ferraro, R., Xie, P. P., Janowiak, J., Rudolf, B., Schneider, U., Curtis, S., Bolvin, D., Gruber, A., Susskind, J., Arkin, P., and Nelkini, E.: The Version 2.1 Global Precipitation Climatology Project (GPCP) Monthly Precipitation Analysis (1979 -Present), J. Hydrometeor., 4(6), 1147-1167, https://doi.org/10.1175/1525-7541(2003)004<1147:TVGPCP>2.0.CO;2, 2003.

Ahn, M.-S., Kim, D., Kang, D., Lee, J., Sperber, K. R., and Glecker, P. J., et al.: MJO propagation across the Maritime Continent: Are CMIP6 models better than CMIP5 models? Geophys. Res. Lett., 47, e2020GL087250, https://doi.org/10.1029/2020GL087250, 2020.

Ahn, M.-S., Kim, D., Sperber, K. R., Kang, I.-S., Maloney, E., Waliser, D., and Hendon, H.: MJO simulation in CMIP5 climate models: MJO skill metrics and process-oriented diagnosis, Clim. Dyn., 49, 4023–4045, https://doi.org/10.1007/s00382-017-3558-4, 2017.

Alappattu, D. P., Wang, Q., Kalogiros, J., Guy, N., and Jorgensen, D. P.: Variability of upper ocean thermohaline structure during a MJO event from DYNAMO aircraft observations, J. Geophys. Res. - Oceans, 122, 1122–1140, https://doi.org/10.1002/2016JC012137, 2017.

Amante, C., and Eakins, B. W.: ETOPO1 1 arc-minute globe relief model: Procedures, data sources and analysis, NOAA Tech. Memo. NESDIS NGDC-24, 19 pp., NOAA, Silver Spring, Md., 2009.

Behringer, D. W., and Xue, Y.: Evaluation of the global ocean data assimilation system at NCEP: The Pacific Ocean. Eighth Symposium on Integrated Observing and Assimilation Systems for Atmosphere, Oceans, and Land Surface, AMS 84th Annual Meeting, Washington State Convention and Trade Center, Seattle, Washington, 11-15. Derber, J.C., and A. Rosati, 1989: A global oceanic data assimilation system, J. Phys. Oceanogr., 19, 1333–1347, https://ams.confex.com/ams/pdfpapers/70720.pdf, 2004.

Bentsen, M., Bethke, I., Debernard, J. B., Iversen, T., Kirkevåg, A., Seland, Ø., Drange, H., Roelandt, C., Seierstad, I. A., Hoose, C., and Kristjánsson, J. E.: The Norwegian Earth System Model, NorESM1-M – Part 1: Description and basic evaluation of the

physical climate, Geosci. Model Dev., 6, 687–720, https://doi.org/10.5194/gmd-6-687-2013, 2013.

Bernie, D., Guilyardi, E., Madec, G., Slingo, J., Woolnough, S., and Cole, J.: Impact of resolving the diurnal cycle in an ocean–atmosphere GCM. Part 2: a diurnally coupled CGCM, Clim. Dynam., 31, 909–925, https://doi.org/10.1007/s00382-008-0429-z, 2008.

Boyle, J. S., Klein, S. A., Lucas, D. D., Ma, H.-Y., Tannahill, J., and Xie, S.: The parametric sensitivity of CAM5's MJO, J. Geophys. Res.-Atmos., 120, 1424–1444, https://doi.org/10.1002/2014JD022507, 2015.

Bui, H. X., and Maloney, E. D.: Changes in Madden-Julian Oscillation precipitation and wind variance under global warming, Geophys. Res. Lett., 45, 7148–7155, https://doi.org/10.1029/2018GL078504, 2018.

Chang, M.-Y., Li, T., Lin, P.-L., and Chang, T.-H.: Forecasts of MJO Events during DYNAMO with a Coupled Atmosphere-Ocean Model: Sensitivity to Cumulus Parameterization Scheme, J. Meteorol. Res., 33**,** 1016–1030, https://doi.org/10.1007/s13351-019-9062-5, 2019.

CLIVAR MADDEN–JULIAN OSCILLATION WORKING GROUP: MJO simulation diagnostics, J. Climate, 22, 3006–3030, https://doi.org/10.1175/2008JCLI2731.1, 2009.

Crueger, T., Stevens, B., and Brokopf, R.: The Madden–Julian Oscillation in ECHAM6 and the introduction of an objective MJO metric, J. Climate, 26, 3241–3257, https://doi.org/10.1175/JCLI-D-12-00413.1, 2013.

Danabasoglu, G., Lamarque, J.-F., Bacmeister, J., Bailey, D. A., DuVivier, A. K., and Edwards, J., et al.: The Community Earth System Model Version 2 (CESM2), J. Adv. Model. Earth Syst., 12, e2019MS001916, https://doi.org/10.1029/2019MS001916, 2020.

Dee, D. P., Uppala, S. M., Simmons, A. J., Berrisford, P., Poli, P., Kobayashi, S., Andrae, U., Balmaseda, M. A., Balsamo, G., Bauer, P., Bechtold, P., Beljaars, A. C. M., van de Berg, L., Bidlot, J., Bormann, N., Delsol, C., Dragani, R., Fuentes, M., Geer, A. J., Haimberger, L., Healy, S. B., Hersbach, H., Hólm, E. V., Isaksen, L., Kållberg, P., Köhler, M., Matricardi, M., McNally, A. P., Monge-Sanz, B. M., Morcrette, J.-J., Park, B.-K., Peubey, C., de Rosnay, P., Tavolato, C., Thépaut, J.-N., and Vitart, F.: The ERA-Interim reanalysis: configuration and performance of the data assimilation system, Q. J. R. Meteorol. Soc., 137: 553–597, https://doi.org/10.1002/qj.828, 2011.

de Szoeke, S. P., Skyllingstad, E. D., Zuidema, P., and Chandra, A. S.: Cold pools and their influence on the tropical marine boundary

794 layer, J. Atmos. Sci., 74, 1149–1168. https://doi.org/10.1175/JAS-
795 D-16-0264.1, 2017.

796 Delworth, T. L., et al.: GFDL's CM2 global coupled climate models.
797 Part 1: Formulation and simulation characteristics, J. Climate, 19,
798 643–674, https://doi.org/10.1175/JCLI3629.1, 2006.

799 DeMott, C. A., Klingaman, N. P., and Woolnough, S. J.: Atmosphere-
800 ocean coupled processes in the Madden-Julian oscillation, Rev.
801 Geophys., 53, 1099–1154, https://doi.org/10.1002/2014RG000478,
802 2015.

803 DeMott, C. A., Klingaman, N. P., Tseng, W.-L., Burt, M. A., Gao, Y.,
804 and Randall, D. A.: The convection connection: How ocean
805 feedbacks affect tropical mean moisture and MJO propagation, J.
806 Geophys. Res.-Atmos., 124, 11,910–11,931,
807 https://doi.org/10.1029/2019JD031015, 2019.

814 Haertel, P.: Prospects for Erratic and Intensifying Madden-Julian
815 Oscillations, Climate, 8, 24, https://doi.org/10.3390/cli8020024,
816 2020.

817 Hannah, W. M., and Maloney, E. D.: The moist static energy budget in
818 NCAR CAM5 hindcasts during DYNAMO, J. Adv. Model. Earth
819 Syst., 6, 420–440, https://doi.org/10.1002/2013MS000272, 2014.

820 Hagos, S. M., Zhang, C., Feng, Z., Burleyson, C. D., Mott, C. De,
821 Kerns, B., Benedict, J. J., and Martini, M. N.: The impact of the
822 diurnal cycle on the propagation of Madden-Julian Oscillation
823 convection across the Maritime Continent, J. Adv. Model. Earth
824 Syst., 8, 1552–1564, https://doi.org/10.1002/2016MS000725, 2016.

825 He, S., Yang, S., and Li, Z.: Influence of Latent Heating over the Asian
826 and Western Pacific Monsoon Region on Sahel Summer
827 Rainfall, Sci. Rep. 7**,** 7680, https://doi.org/10.1038/s41598-017-
828 07971-6, 2017.

829 Heath, A., Gonzalez, A. O., Gehne, M., and Jaramillo, A.: Interactions
830 of large-scale dynamics and Madden-Julian Oscillation propagation
831 in multi-model simulations, J. Geophys. Res.-Atmos., 126,
832 e2020JD033988. https://doi.org/10.1029/2020JD033988, 2021.

833 Hong, X., Reynolds, C. A., Doyle, J. D., May, P., and O'Neill, L.:
834 Assessment of upper-ocean variability and the Madden-Julian
835 Oscillation in extended-range air–ocean coupled mesoscale
836 simulations, Dyn. Atmos. Oceans, 78, 89–105.
837 https://doi.org/10.1016/j.dynatmoce.2017.03.002, 2017.

838 Hung, M.-P., Lin, J.-L., Wang, W., Kim, D., Shinoda, T., and Weaver,
839 S. J.: MJO and convectively coupled equatorial waves simulated by
840 CMIP5 climate models, J. Climate, 26, 6185–6214,
841 https://doi.org/10.1175/JCLI-D-12-00541.1, 2013.

842 Hurrell, J. W., Holland, M. M., Gent, P. R., Ghan, S., Kay, J. E.,

Kushner, P. J., Lamarque, J.-F., Large, W. G., Lawrence, D., Lindsay, K., Lipscomb, W. H., Long, M. C., Mahowald, N., Marsh, D. R., Neale, R. B., Rasch, P., Vavrus, S., Vertenstein, M., Bader, D., Collins, W. D., Hack, J. J., Kiehl, J., and Marshall, S.: The community Earth system model: A framework for collaborative research, B. Am. Meteorol. Soc., 94, 1319–1360, https://doi.org/10.1175/BAMS-D-12-00121, 2013.

Jiang, X., et al.: Vertical structure and physical processes of the MaddenJulian oscillation: Exploring key model physics in climate simulations, J. Geophys. Res.-Atmos., 120, 4718–4748, https://doi.org/10.1002/2014JD022375, 2015.

Jiang, X., Adames, Á. F., Kim, D., Maloney, E. D., Lin, H., and Kim, H., et al.: Fifty years of research on the Madden-Julian Oscillation: Recent progress, challenges, and perspectives, J. Geophys. Res.-Atmos., 125, e2019JD030911, https://doi.org/10.1029/2019JD030911, 2020.

Johnson, R. H., and Ciesielski, P. E.: Multiscale variability of the atmospheric boundary layer during DYNAMO, J. Atmos. Sci., 74, 4003–4021, https://doi.org/10.1175/JAS-D-17-0182.1, 2017.

Kaylor, R. E.: Filtering and decimation of digital time series, Tech. Rep. Note BN 850, Institute for Physical Science and Technology, University of Maryland at College Park, 14 pp., 1977.

Kim, D., Sobel, A. H., Maloney, E. D., Frierson, D. M., and Kang, I.-S.: A systematic relationship between intraseasonal variability and mean state bias in AGCM simulations, J. Climate, 24, 5506–5520. https://doi.org/10.1175/2011JCLI4177.1, 2011.

Kim, D., Kim H., and Lee, M.-I.: Why does the MJO detour the Maritime Continent during austral summer? Geophys. Res. Lett., 44, 2579–2587, https://doi.org/10.1002/2017GL072643, 2017.

Kim, H.-M., Hoyos, C. D., and Webster, P. J. et al.: Ocean–atmosphere coupling and the boreal winter MJO, Clim Dynam., 35, 771–784, https://doi.org/10.1007/s00382-009-0612-x, 2010.

Kiranmayi, L., and Maloney, E. D.: Intraseasonal moist static energy budget in reanalysis data, J. Geophys. Res., 116, D21117, https://doi.org/10.1029/2011JD016031, 2011.

Lan, Y.-Y., Tsuang, B.-J., Tu, C.-Y., Wu, T.-Y., Chen, Y.-L., and Hsieh, C.-I.: Observation and Simulation of Meteorology and Surface Energy Components over the South China Sea in Summers of 2004 and 2006, Terr. Atmos. Ocean. Sci., 21, 325–342, https://doi.org/ 10.3319/TAO.2009.04.07.01(A), 2010.

Lee, H.-T., and NOAA CDR Program: NOAA Climate Data Record (CDR) of Daily Outgoing Longwave Radiation (OLR), Version 1.2, NOAA National Climatic Data

887 Center, https://doi.org/10.7289/V5SJ1HH2, 2011.

888 Li, T., Ling, J., and Hsu, P.-C.: Madden–Julian Oscillation: Its
889 discovery, dynamics, and impact on East Asia, J. Meteor. Res., 34,
890 20–42, https://doi.org/10.1007/s13351-020-9153-3, 2020.

891 Li, T., Tam, F., Fu, X., Zhou, T., and Zhu, W.: Causes of the
892 intraseasonal SST variability in the tropical Indian Ocean, Atmos.
893 Oceanic Sci. Lett., 1, 18–23,
894 https://doi.org/10.1080/16742834.2008.11446758, 2008.

895 Li, X., Tang, Y., Zhou, L., Chen, D., and Yao, Z.: Assessment of Madden–Julian
896 oscillation simulations with various configurations of CESM, Clim. Dynam.,
897 47, 2667–2690, https://doi.org/10.1007/s00382-016-2991-0, 2016.

898 Ling, J., Zhao, Y., and Chen, G.: Barrier effect on MJO propagation by
899 the Maritime Continent in the MJO Task Force/GEWEX
900 atmospheric system study models, J. Climate, 32, 5529–
901 5547, https://doi.org/10.1175/JCLI-D-18-0870.1, 2019.

902 Madden, R. A., and Julian, P. R.: Description of global-scale
903 circulation cells in the tropics with a 40-50 day period, J. Atmos.
904 Sci., 29, 1109-1123, https://doi.org/10.1175/1520-
905 0469(1972)029<1109:DOGSCC>2.0.CO;2, 1972.

906 Madden, R. A., and Julian, P. R.: Observations of the 40-50 day
907 tropical oscillation - A review, Mon. Weather Rev., 122, 814– 837,
908 https://doi.org/10.1175/1520-
909 0493(1994)122<0814:OOTDTO>2.0.CO;2, 1994.

910 Neale, R. B., et al.,: Description of the NCAR Community Atmosphere
911 Model (CAM 5.0), NCAR Tech. Note NCAR/TN-486+STR, 289
912 pp., Natl. Cent. for Atmos. Res, Boulder, Colo., 2012.

913 Newman, M., Sardeshmukh, P. D., and Penland, C.: How important is
914 air–sea coupling in ENSO and MJO evolution? J.
915 Clim., 22, 2958– 2977, https://doi.org/10.1175/2008JCLI2659.1,
916 2009.

917 Oh, J., Kim, B., and Kim, K. et al.: The impact of the diurnal cycle on
918 the MJO over the Maritime Continent: a modeling study
919 assimilating TRMM rain rate into global analysis, Clim.
920 Dynam., 40, 893–911, https://doi.org/10.1007/s00382-012-1419-8,
921 2013.

922 Pei, S., Shinoda, T., Soloviev, A., and Lien, R.-C.: Upper ocean
923 response to the atmospheric cold pools associated with the
924 Madden-Julian Oscillation, Geophys. Res. Lett., 45, 5020–5029,
925 https://doi.org/10.1029/2018GL077825, 2018.

926 Pujiana, K., Moum, J. N., and Smyth, W. D.: The role of subsurface
927 turbulence in redistributing upper-ocean heat, freshwater, and
928 momentum in response to the MJO in the equatorial Indian
929 Ocean, J. Phys. Oceanogr., 48, 197–

220, https://doi.org/10.1175/JPO-D-17-0146.1, 2018.

Rayner, N. A., Parker, D. E., Horton, E. B., Folland, C. K., Alexander, L. V., Rowell, D. P., Kent, E. C., and Kaplan, A.: Global analyses of sea surface temperature, sea ice, and night marine air temperature since the late nineteenth century, J. Geophys. Res., 108(D14), 4407, https://doi.org/10.1029/2002JD002670, 2003.

Ren, P. F., Gao, L., and Ren, H.-L. et al.: Representation of the Madden–Julian Oscillation in CAMSCSM, J. Meteor. Res., 33, 627–650, https://doi.org/10.1007/s13351-019-8118-x, 2019.

Reynolds, R. W., and Smith, T. M.: A high-resolution global sea surface temperature climatology, J. Clim., 8(6),1571–1583, https://doi.org/10.1175/1520-0442(1995)008<1571:AHRGSS>2.0.CO;2, 1995.

Schreck, C. J., Lee, H.-T., and Knapp, K. R.: HIRS outgoing longwave radiation—Daily climate data record: Application toward identifying tropical subseasonal variability, Remote Sens., 10, 1325. https://doi.org/10.3390/rs10091325, 2018.

Sobel, A. H., Maloney, E. D., Bellon, G., and Dargan, M. F.: The role of surface heat fluxes in tropical intraseasonal oscillations, Nat. Geosci., 1, 653–657, https://doi.org/10.1038/ngeo312, 2008.

Subramanian, A. C., Jochum, M., Miller, A. J., Murtugudde, R., Neale, R. B., and Waliser, D. E.: The Madden–Julian oscillation in CCSM4, J. Climate, 24, 6261–6282, https://doi.org/10.1175/JCLI-D-11-00031.1, 2011.

Tseng, W.-L., Tsuang, B.-J., Keenlyside, N. S., Hsu, H.-H. and Tu, C.-Y.: Resolving the upper-ocean warm layer improves the simulation of the Madden-Julian oscillation, Clim. Dynam., 44, 1487–1503, https://doi.org/10.1007/s00382-014-2315-1, 2014.

Tseng, W.-L., Hsu, H.-H., Keenlyside, N., Chang, C.-W. J., Tsuang, B.-J., Tu, C.-Y., and Jiang, L.-C.: Effects of Orography and Land–Sea Contrast on the Madden–Julian Oscillation in the Maritime Continent: A Numerical Study Using ECHAM-SIT, J. Climate, 30, 9725–9741, https://doi.org/10.1175/JCLI-D-17-0051.1, 2017.

Tu, C.-Y., and Tsuang, B.-J.: Cool-skin simulation by a one-column ocean model, Geophys. Res. Lett., 32, L22602, https://doi.org/10.1029/2005GL024252, 2005.

Wang, W., Saha, S., Pan, H.-L., Nadiga, S., and White, G.: Simulation of ENSO in the new NCEP Coupled Forecast System Model (CFS03), Mon. Wea. Rev., 133, 1574–1593, https://doi.org/10.1175/MWR2936.1, 2005.

Wang, W., Hung, M.-P., Weaver, S. J., Kumar, A., and Fu, X.: MJO prediction in the NCEP Climate Forecast System version 2, Clim. Dyn., 42, 2509–2520, https://doi.org/10.1007/s00382-013-1806-9,

2014.

Wheeler, M. C., and Hendon, H. H.: An all-season real-time multivariate MJO index: development of an index for monitoring and prediction, Mon. Weather Rev., 132, 1917–1932, https://doi.org/10.1175/1520-0493(2004)132<1917:AARMMI>2.0.CO;2, 2004.

Wheeler, M., and Kiladis, G. N.: Convectively coupled equatorial waves: Analysis of clouds and temperature in the wavenumber-frequency domain, J. Atmos. Sci., 56, 374– 399, https://doi.org/10.1175/1520-0469(1999)056<0374:CCEWAO>2.0.CO;2, 1999.

Woolnough, S. J., Vitard, F., and Balmaseda, M. A.: The role of the ocean in the Madden–Julian oscillation: Implications for MJO prediction, Quart. J. Roy. Meteor. Soc., 133, 117–128, https://doi.org/10.1002/qj.4, 2007.

Wu, C.-H., and Hsu, H.-H.: Potential Influence of Topography on the MJO in the Maritime Continent, J. Climate, 22, 5433–5448, https://doi.org/10.1175/2009JCLI2825.1, 2009.

Yoneyama, K., Zhang, C., and Long, C.: Tracking pulses of the Madden–Julian oscillation, Bull. Amer. Meteor. Soc., 94, 1871–1891, https://doi.org/10.1175/BAMS-D-12-00157.1, 2013.

Zhang, C.: Madden-Julian oscillation, Rev. Geophys., 43, RG2003, https://doi.org/10.1029/2004RG000158, 2005.

Zhang, C., and Yoneyama, K.: CINDY/DYNAMO field campaign: Advancing our understanding of MJO initiation, In World Scientific Series on Asia-Pacific Weather and Climate (pp. 339-348). (World Scientific Series on Asia-Pacific Weather and Climate; Vol. Volume 9), World Scientific Publishing Co. Pte Ltd. https://doi.org/10.1142/9789813200913_0027, 2017.

1002 Table 1. List of experiments

Section	Category	Experiments	Description
3.1	Coupled or uncoupled	A–CTL	Standalone CAM5.3 forced by forced by the monthly mean Hadley Centre SST dataset version 1 climatology
		C–30NS (the control coupled experiment)	CAM5.3 coupled with SIT over the tropical domain (30°N–30°S), with 41 layers of finest vertical resolution (up to the seabed) and diurnal cycle; the frequency of CAM5 being exchanged with CPL is 48 times per day
3.2	Upper-ocean vertical resolution	C–LR12m	The first ocean vertical level starts at 11.5 m with 31 layers (beside SST and cool skin layer are 11.5 m, 29.5 m and 43.6 m up to the seabed)
		C–LR34m	The first ocean vertical level starts at 33.9 m with 28 layers (beside SST and cool skin layer are 33.9 m, 76.9 m and 96.8 m up to the seabed)
3.3	Lowest boundary of SIT	C–HR1mB10m	The lowest boundary of SIT has a depth of 10 m (model depth between 0 m and 10 m)
		C–HR1mB30m	The lowest boundary of SIT has a depth of 30 m (model depth between 0 m and 30 m)
		C–HR1mB60m	The lowest boundary of SIT has a depth of 60 m (model depth between 0 m and 60 m)
3.4	Regional coupling domain in latitude	C–0_30N	Coupled in the tropical northern hemisphere (0°N–30°N, 0°E–360°E)
		C–0_30S	Coupled in the tropical southern hemisphere (0°S–30°S, 0°E–360°E)
	Regional coupling domain in longitude	C–30_180E	Coupled in the Indo-Pacific (30°N–30°S, 30°E–180°E)
		C–30E_75W	Coupled over the Indian Ocean and Pacific Ocean (30°N–30°S, 30°E–75°W)
3.5	Absence of the diurnal cycle	C–30NS–nD	Absence of the diurnal cycle in C–30NS; the CAM5.3 daily atmospheric mean of surface wind, temperature, total precipitation, net surface heat flux, u-stress and v-stress over water trigger the SIT and daily mean SST feedback to atmosphere; the frequency of CAM5 is exchanged with CPL 48 times per day

1003 Experiment abbreviations: “A” means standalone AGCM simulation. “C” means the
1004 CAM5.3 coupled to the SIT model.

Figure List

Figure 1. Schematics of coupled and uncoupled domains in the regional coupling experiment: (a) C–30NS, (b) C–0_30N, (c) C–0_30S, (d) C–30_180E, and (e) C–30E_75W. The background is the climatological mean SST in December–February (DJF).

Figure 2. (a)–(c) Zonal wavenumber–frequency spectra for 850-hPa zonal wind averaged over 10°S–10°N in boreal winter after removing the climatological mean seasonal cycle. Vertical dashed lines represent periods at 80 and 30 days, respectively. (d)–(f) Hovmöller diagrams of the correlation between the precipitation averaged over 10°S–5°N, 75–100°E and the intraseasonally filtered precipitation (color) and 850-hPa zonal wind (contour) averaged over 10°N–10°S. (g)–(i) Zonal wavenumber–frequency power spectra of anomalous OLR (colors) and phase lag with U850 (vectors) for the symmetric component of tropical waves, with the vertically upward vector representing a phase lag of 0° with phase lag increasing clockwise. Three dispersion straight lines with increasing slopes represent the equatorial Kelvin waves (derived from the shallow water equations) corresponding to three equivalent depths, 12, 25, and 50 m, respectively. (j)–(l) Composites of 20–100-day filtered OLR (W m^{-2}, shaded) and 850-hPa wind (m s^{-1}, vector) for MJO phase 5 when deep convection is the strongest over the MC and 850-hPa wind, with the reference vector (1 m s^{-1}) shown at the top right of each panel, and (m)–(o) 15°N–15°S averaged p-vertical velocity anomaly (Pa s^{-1}, shaded) and moist static energy tendency anomaly (W m^{-2}, contour, interval 0.003); solid, dashed, and thick-black lines represent positive, negative, and zero values, respectively. The number of days used to generate the composite is shown at the bottom right corner of each panel. (a), (d), (g), (j), and (m) are from the ERA-Interim and NOAA post-processed data (abbr. ERA-I/NOAA); (b), (e), (h), (k), and (n) are from the control experiment C–30NS; and (c), (f), (i), (l), and (o) are from the A–CTL.

Figure 3. Evolution of the filtered OLR anomaly (W m^{-2}, shaded) and 850-hPa wind (m s^{-1}, vector) at phase 2, 4, 6, and 8: (a) the ERA-I/NOAA data, (b) the control coupled experiment C–30NS, and (c) the uncoupled experiment A–CTL. The unit of the reference vector shown at the top right corner of each panel is m s^{-1}, and the number of days used for the composite is shown at the bottom right corner of each panel.

Figure 4. (a)–(c) Phase-longitude Hovmöller diagrams of 20–100-day filtered precipitation (mm day^{-1}, shaded) and SST anomaly (K, contour) averaged over 10°N–10°S from phase 1 to 8. Contour interval is 0.03; solid, dashed, and thick-black lines represent positive, negative, and zero values, respectively. (d)–(f) Phase-vertical Hovmöller diagrams of 20–100-day moisture divergence (shading, 10^{-6} g kg^{-1} s^{-1}) and

zonal wind (contoured, m s^{-1}) averaged over 10°N–10°S, 120–150°E; solid, dashed, and thick-black curves are positive, negative, and zero values, respectively. (g)–(i) Variation of 30–60-day filtered precipitation in the eastern IO and the WP in observation (color shading), and the ratio between intraseasonal and total variance (contoured) and (j)–(l) composites 20–100-day filtered SST (K, shaded) and 850-hPa winds (m s^{-1}, vector) at phase 7 when deep convection was the strongest over the dateline. Reference vector shown at the top right corner of each panel. (a), (d), (g), and (j) are from the ERA-I/NOAA data; (b), (e), (h), and (k) are from the control coupled experiment C–30NS; and (c), (f), (i), and (l) are from the uncoupled experiment A–CTL.

Figure 5. Composites of 20–100-day filtered oceanic temperature (K, shaded) between 0 and 60 m depth for MJO phase 1, 3, 5, and 7 (shown at the lower right corner of each panel) in C–30NS, C–LR12m and C–LR34m.

Figure 6. (a)–(b) Same as in Fig. 2(a) but for the C–LR12m and C–LR34m. (c)–(d) Same as in Fig. 2(d) but for the C–LR12m and C–LR34m. (e)–(f) Same as in Fig. 4(a) but for the C–LR12m and C–LR34m.

Figure 7. Same as in Fig. 6 but for the C–HR1mB10m, C–HR1mB30m, and C–HR1mB60m.

Figure 8. Same as in Fig. 6 but for the C–0_30N, C–0_30S, C–30_180E, and C–30E_75W.

Figure 9. Same as in Fig. 3 but for phase 5 in the C–0_30N, C–0_30S, C–30_180E, and C–30E_75W.

Figure 10. Similar as in Fig. 6 but for the C–30NS–nD.

Figure 11. Scattered plots of various MJO indices in the ERA-I/NOAA data and 12 experiments: (a) power ratio of east/west propagating waves of wavenumber 1–3 of 850-hPa zonal winds (X-axis) with a 30–80-day period and eastward propagation speed of U850 anomaly (Y-axis) from the Hovmöller diagram and (b) RMM1 and RMM2 variance and eastward propagation speed of the filtered precipitation anomaly derived from the Hovmöller diagram.

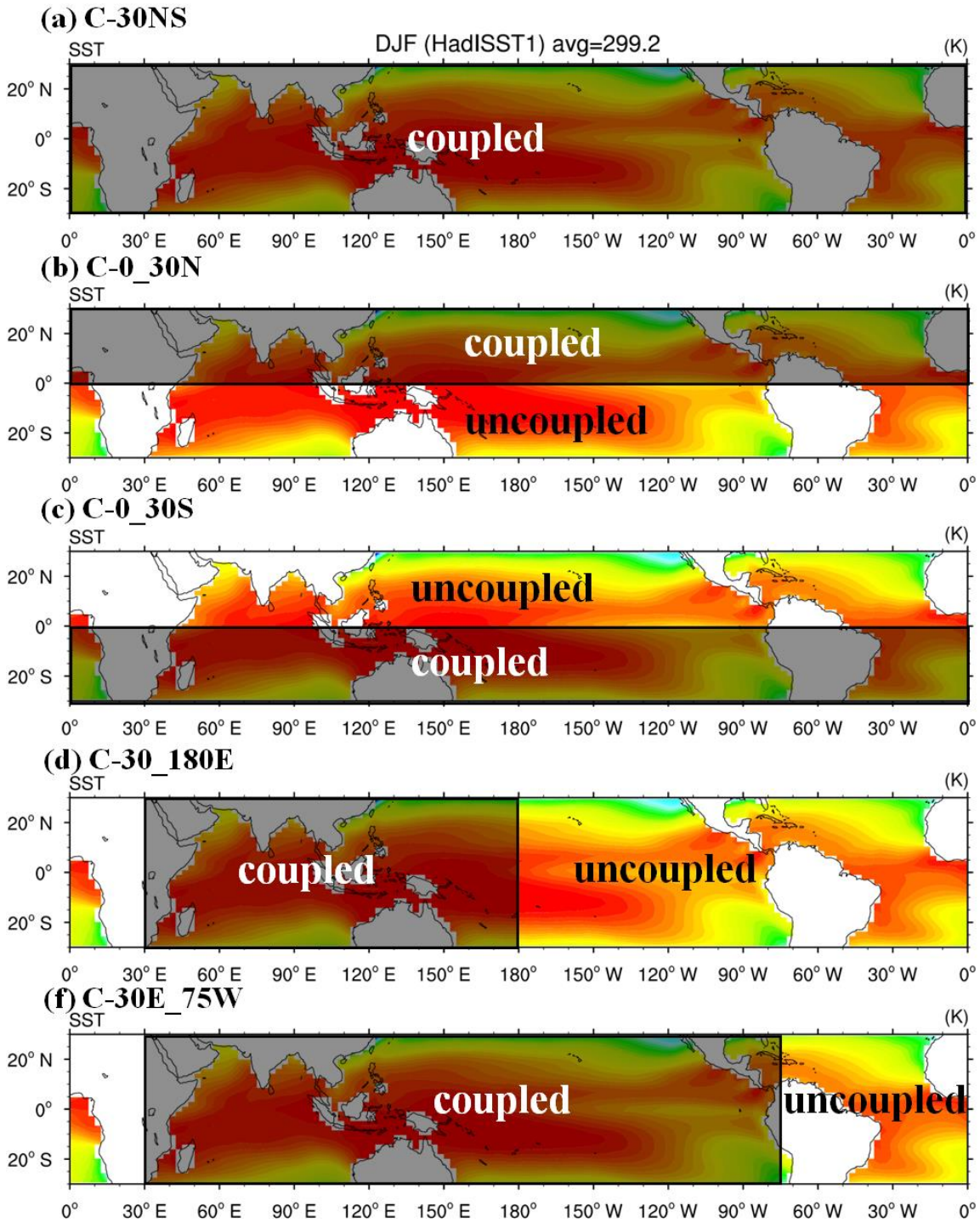

Figure 1. Schematics of coupled and uncoupled domains in the regional coupling experiment: (a) C–30NS, (b) C–0_30N, (c) C–0_30S, (d) C–30_180E, and (e) C–30E_75W. The background is the climatological mean SST in December–February (DJF).

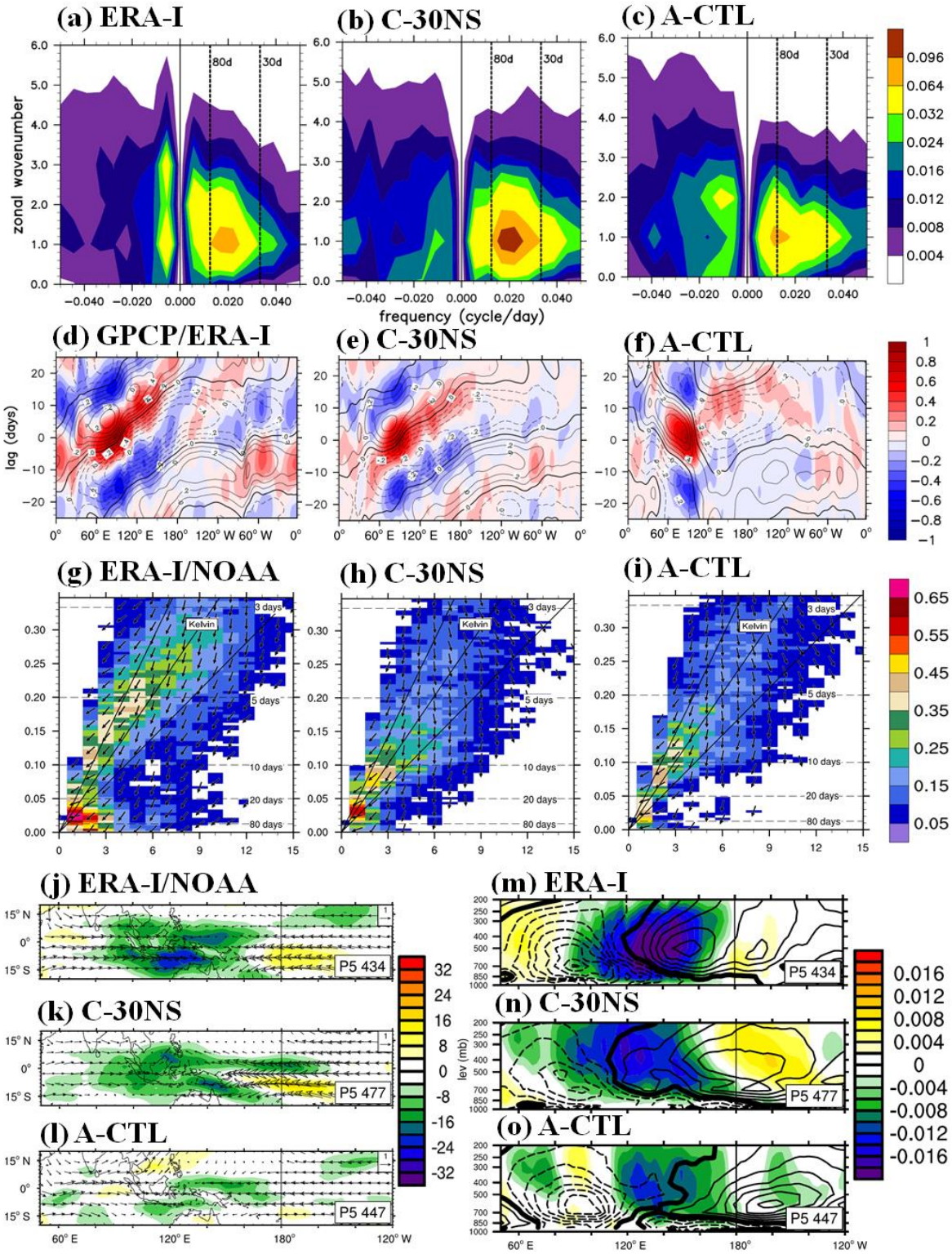

Figure 2. (a)–(c) Zonal wavenumber–frequency spectra for 850-hPa zonal wind averaged over 10°S–10°N in boreal winter after removing the climatological mean seasonal cycle. Vertical dashed lines represent periods at 80 and 30 days, respectively. (d)–(f) Hovmöller

diagrams of the correlation between the precipitation averaged over 10°S–5°N, 75–100°E and the intraseasonally filtered precipitation (color) and 850-hPa zonal wind (contour) averaged over 10°N–10°S. (g)–(i) Zonal wavenumber–frequency power spectra of anomalous OLR (colors) and phase lag with U850 (vectors) for the symmetric component of tropical waves, with the vertically upward vector representing a phase lag of 0° with phase lag increasing clockwise. Three dispersion straight lines with increasing slopes represent the equatorial Kelvin waves (derived from the shallow water equations) corresponding to three equivalent depths, 12, 25, and 50 m, respectively. (j)–(l) Composites of 20–100-day filtered OLR (W m^{-2}, shaded) and 850-hPa wind (m s^{-1}, vector) for MJO phase 5 when deep convection is the strongest over the MC and 850 hPa wind, with the reference vector (1 m s^{-1}) shown at the top right of each panel, and (m)–(o) 15°N–15°S averaged p-vertical velocity anomaly (Pa s^{-1}, shaded) and moist static energy tendency anomaly (W m^{-2}, contour, interval 0.003); solid, dashed, and thick-black lines represent positive, negative, and zero values, respectively. The number of days used to generate the composite is shown at the bottom right corner of each panel. (a), (d), (g), (j), and (m) are from the ERA-Interim and NOAA post-processed data (abbr. ERA-I/NOAA); (b), (e), (h), (k), and (n) are from the control experiment C–30NS; and (c), (f), (i), (l), and (o) are from the A–CTL.

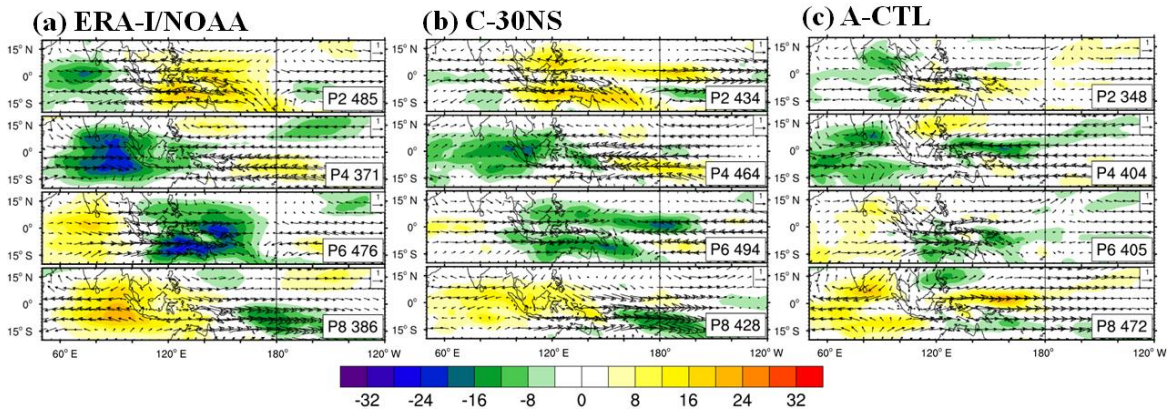

Figure 3. Evolution of the filtered OLR anomaly (W m^{-2}, shaded) and 850-hPa wind (m s^{-1}, vector) at phase 2, 4, 6, and 8: (a) the ERA-I/NOAA data, (b) the control coupled experiment C–30NS, and (c) the uncoupled experiment A–CTL. The unit of the reference vector shown at the top right corner of each panel is m s^{-1}, and the number of days used for the composite is shown at the bottom right corner of each panel.

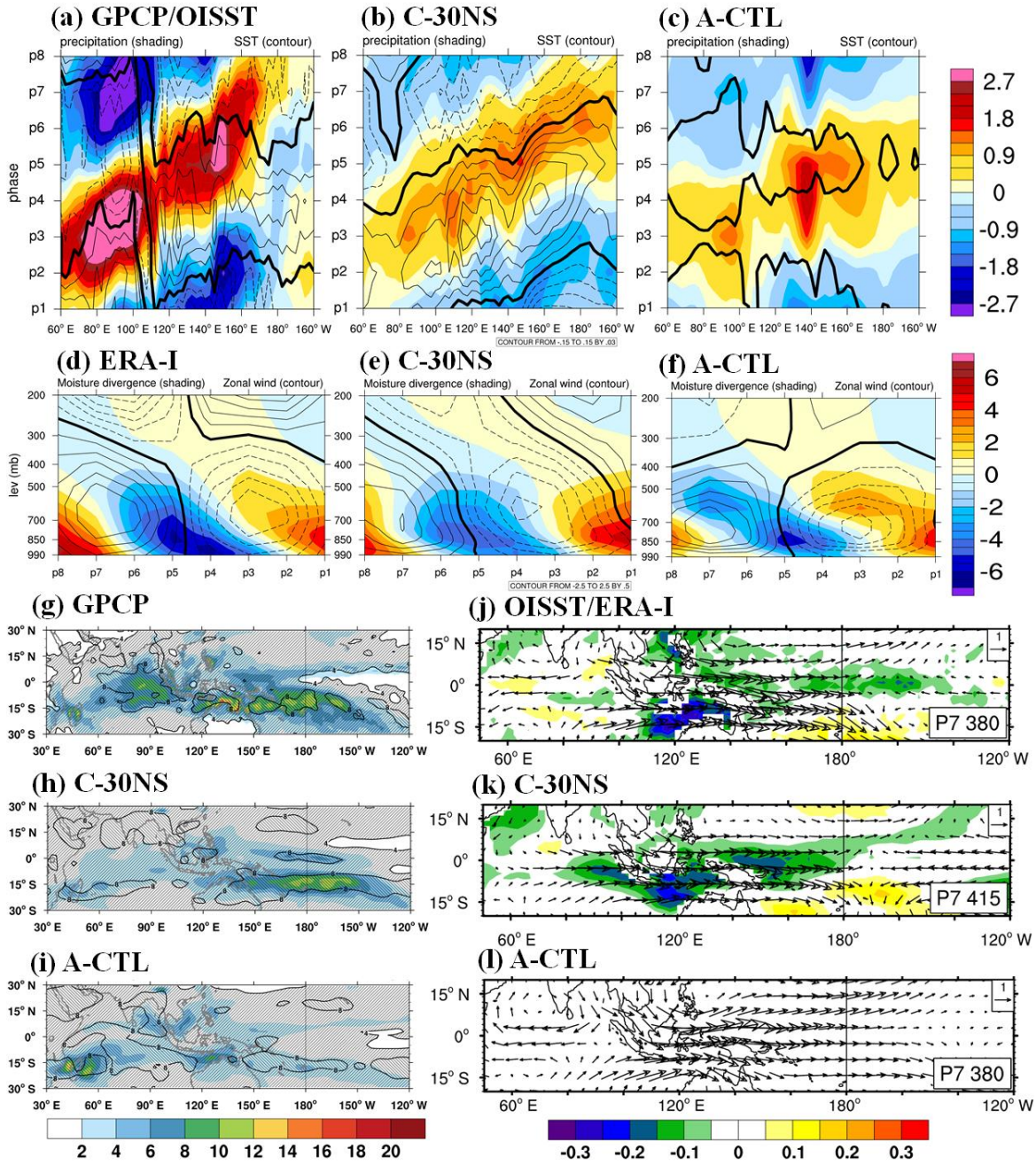

1114

1115

1116 **Figure 4.** (a)–(c) Phase-longitude Hovmöller diagrams of 20–100-day filtered
1117 precipitation (mm day^{-1}, shaded) and SST anomaly (K, contour) averaged over 10°N–
1118 10°S from phase 1 to 8. Contour interval is 0.03; solid, dashed, and thick-black lines
1119 represent positive, negative, and zero values, respectively. (d)–(f) Phase-vertical
1120 Hovmöller diagrams of 20–100-day moisture divergence (shading, 10^{-6} g kg^{-1} s^{-1}) and
1121 zonal wind (contoured, m s^{-1}) averaged over 10°N–10°S, 120–150°E; solid, dashed, and
1122 thick-black curves are positive, negative, and zero values, respectively. (g)–(i) Variation
1123 of 30–60-day filtered precipitation in the eastern IO and the WP in observation (color
1124 shading), and the ratio between intraseasonal and total variance (contoured) and (j)–(l)

composites 20–100-day filtered SST (K, shaded) and 850-hPa winds (m s^{-1}, vector) at phase 7 when deep convection was the strongest over the dateline. Reference vector shown at the top right corner of each panel. (a), (d), (g), and (j) are from the ERA-I/NOAA data; (b), (e), (h), and (k) are from the control coupled experiment C–30NS; and (c), (f), (i), and (l) are from the uncoupled experiment A–CTL.

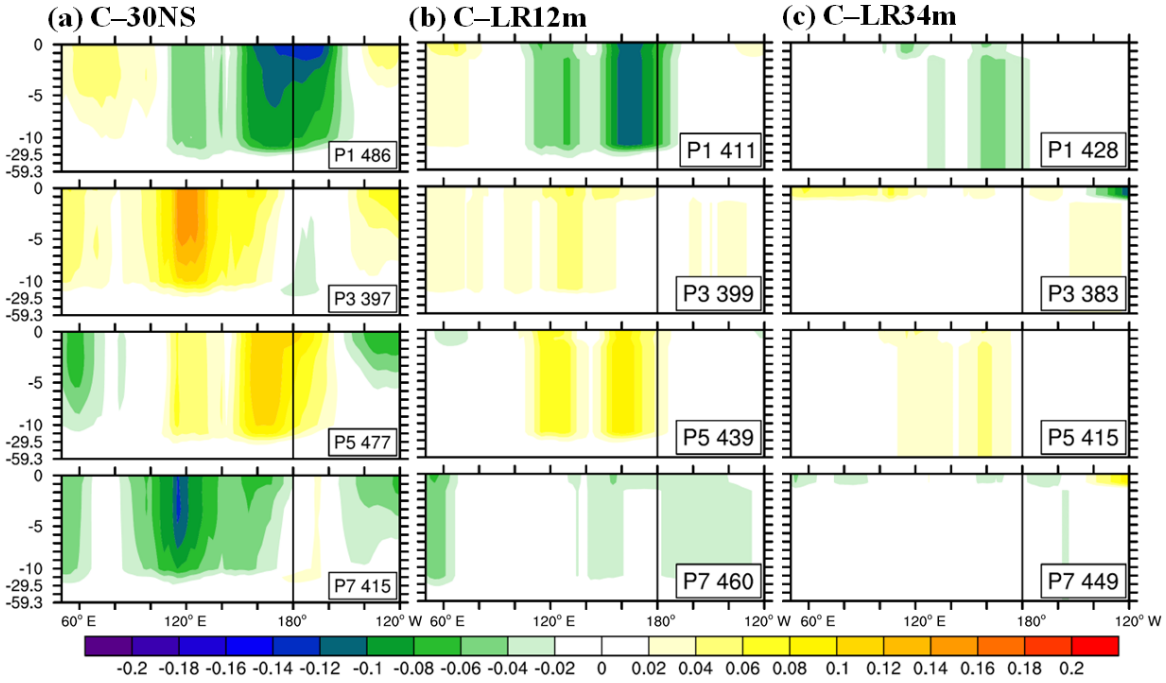

Figure 5. Composites of 20–100-day filtered oceanic temperature (K, shaded) between 0 and 60 m depth for MJO phase 1, 3, 5, and 7 (shown at the lower right corner of each panel) in C–30NS, C–LR12m and C–LR34m.

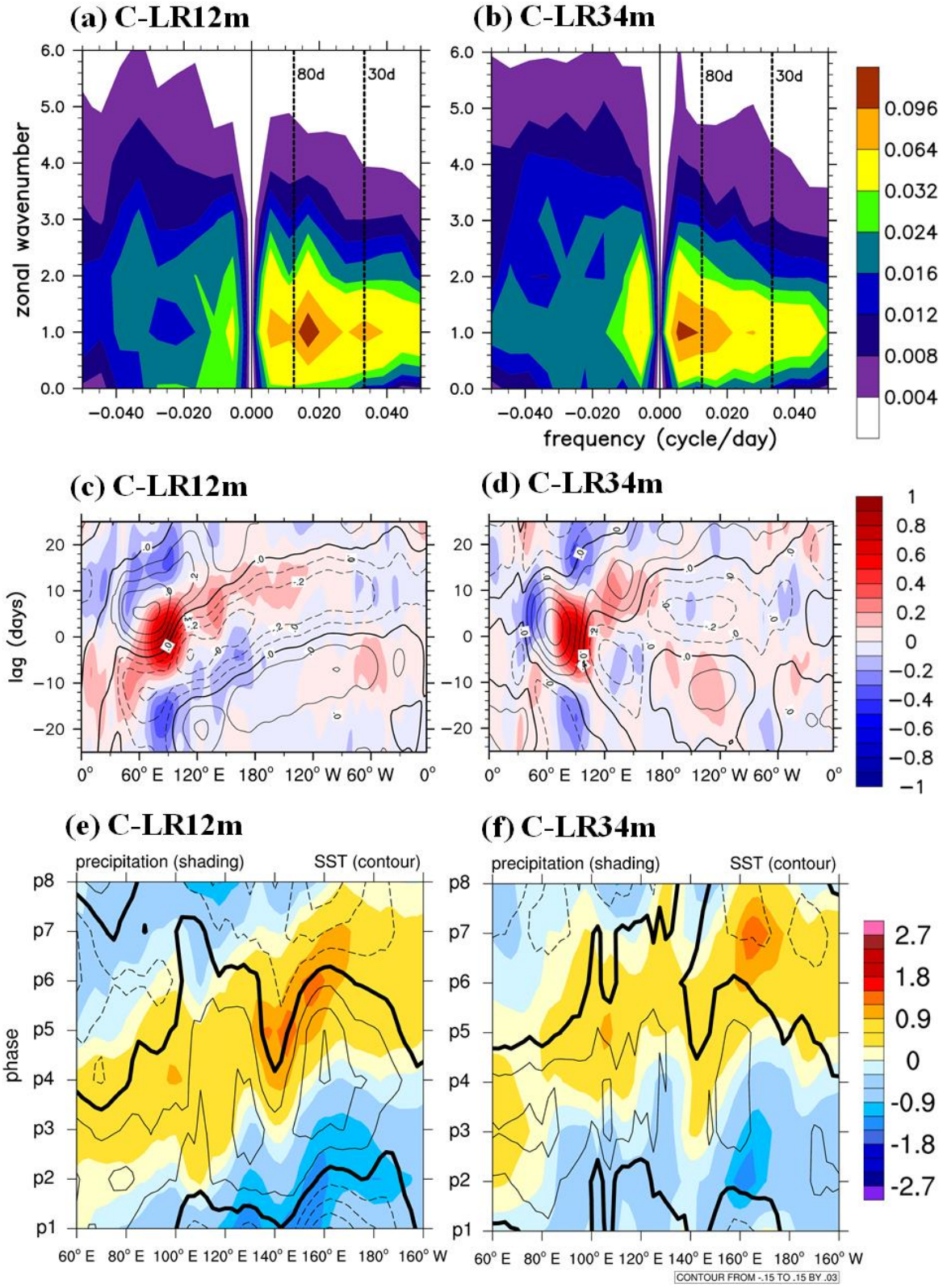

Figure 6. (a)–(b) Same as in Fig. 2(a) but for the C–LR12m and C–LR34m. (c)–(d) Same as in Fig. 2(d) but for the C–LR12m and C–LR34m. (e)–(f) Same as in Fig. 4(a) but for the C–LR12m and C–LR34m.

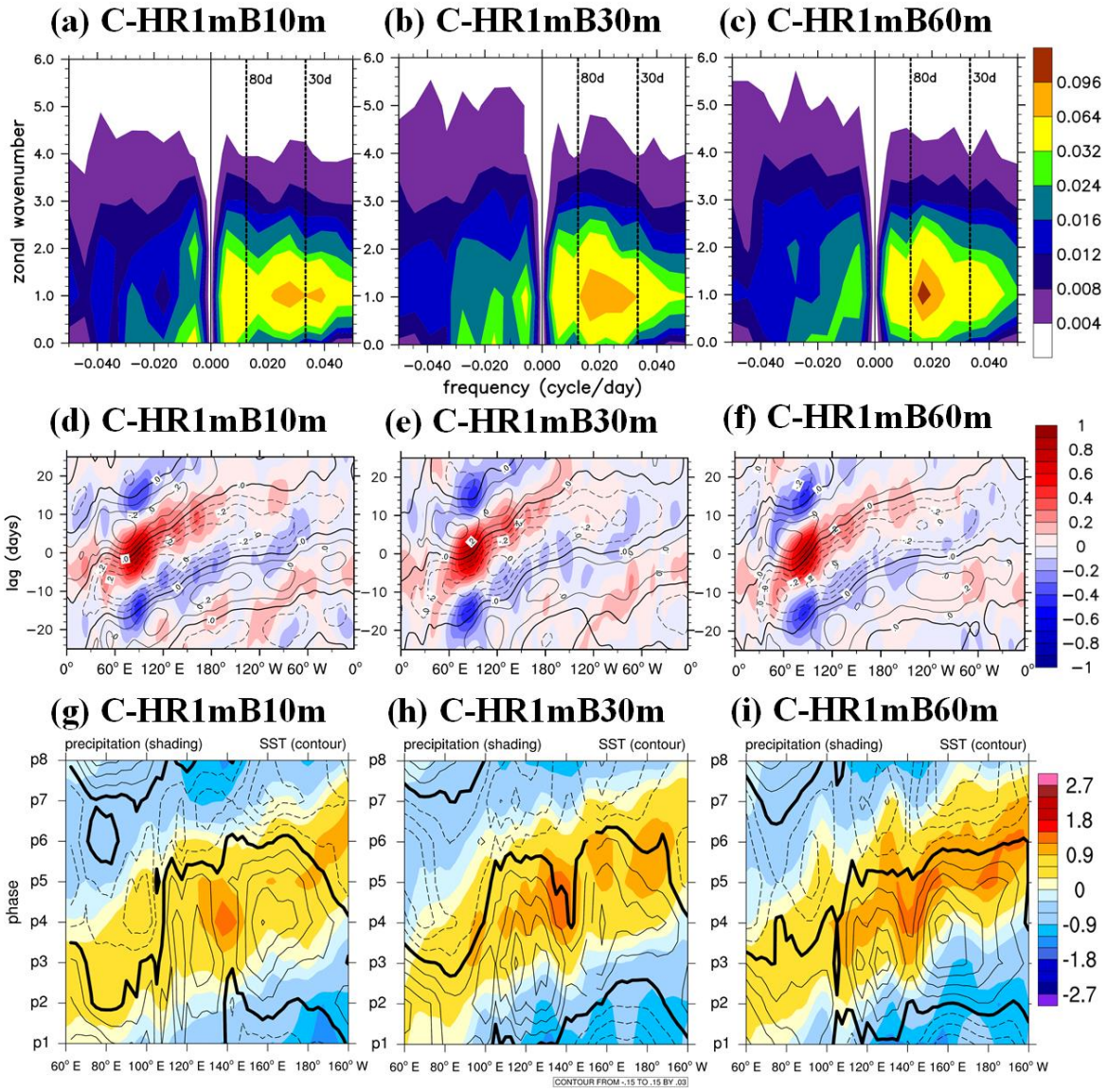

Figure 7. Same as in Fig. 6 but for the C–HR1mB10m, C–HR1mB30m, and C–HR1mB60m.

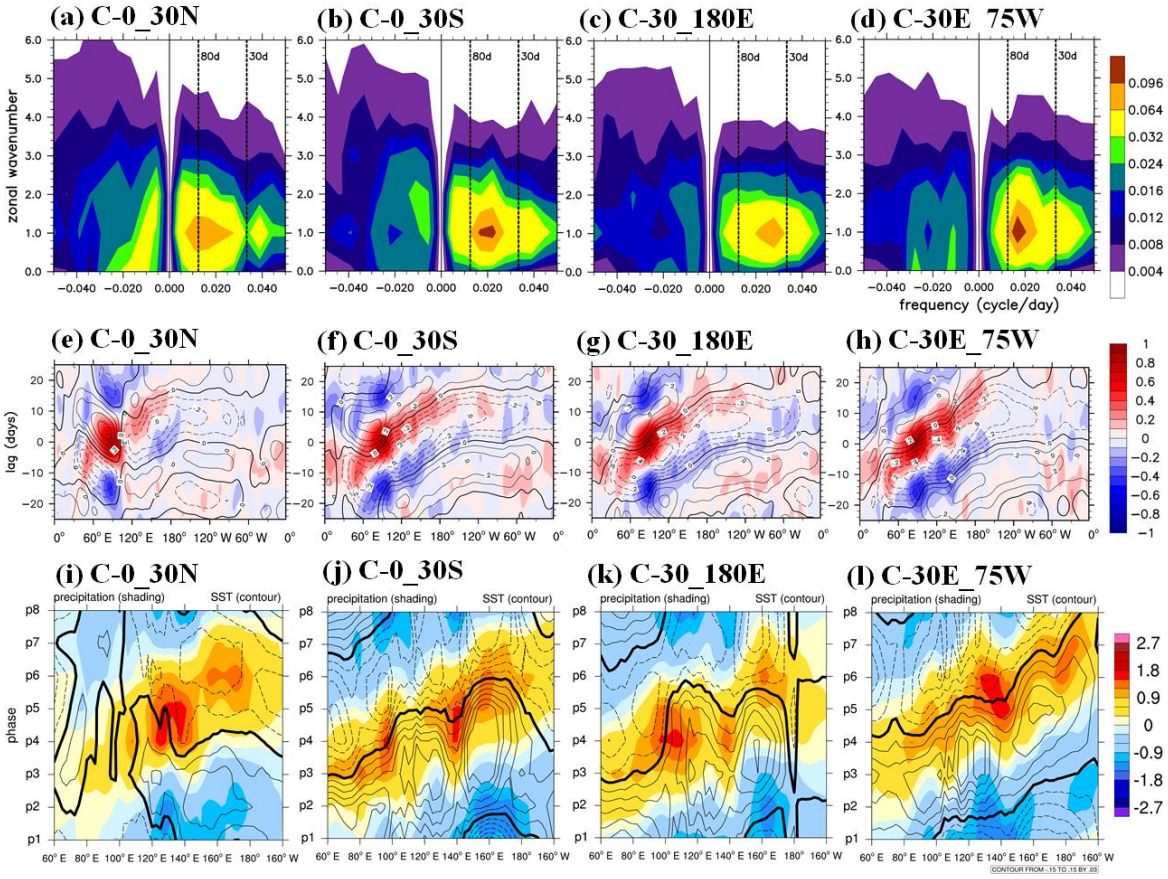

Figure 8. Same as in Fig. 6 but for the C–0_30N, C–0_30S, C–30_180E, and C–30E_75W.

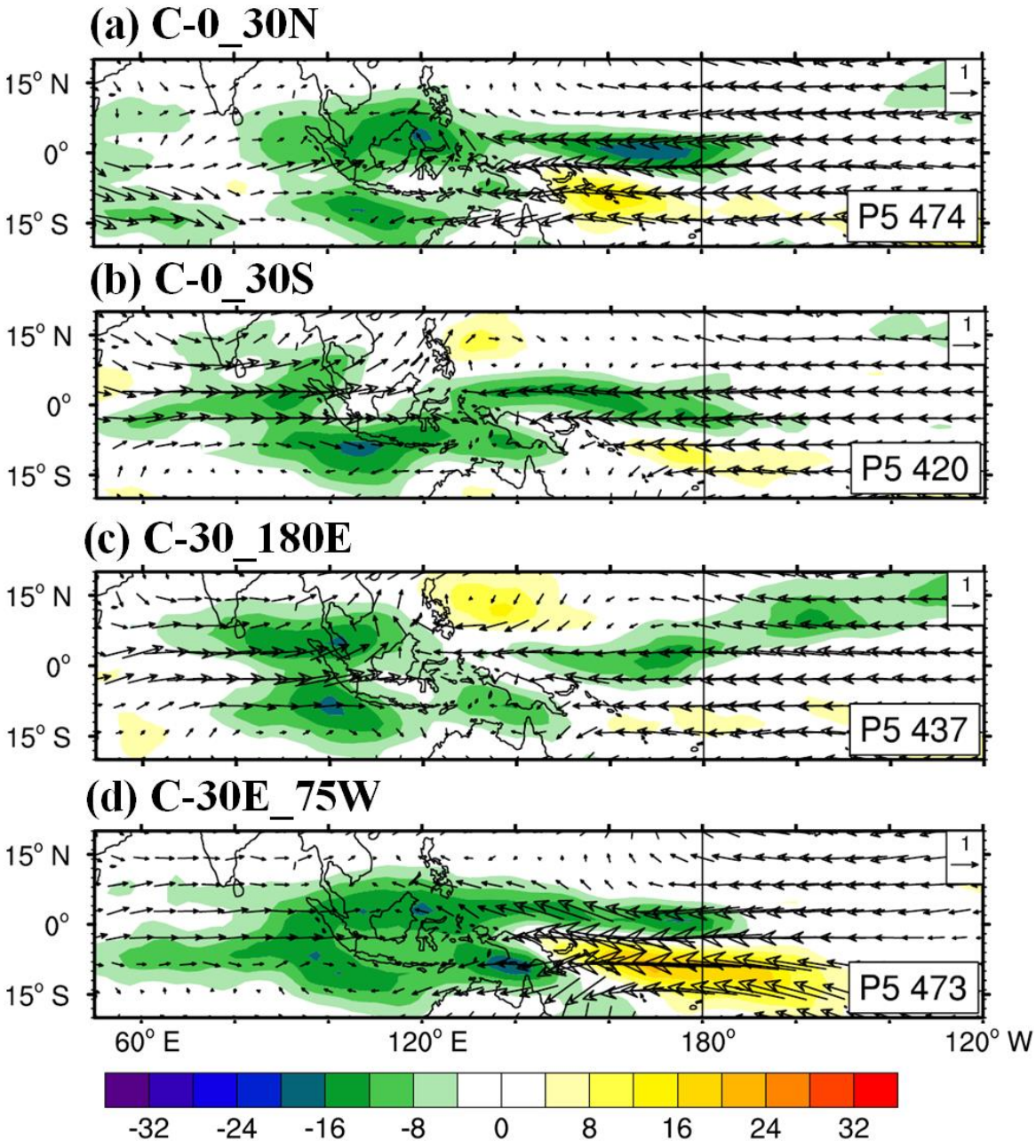

Figure 9. Same as in Fig. 3 but for phase 5 in the C–0_30N, C–0_30S, C–30_180E, and C–30E_75W.

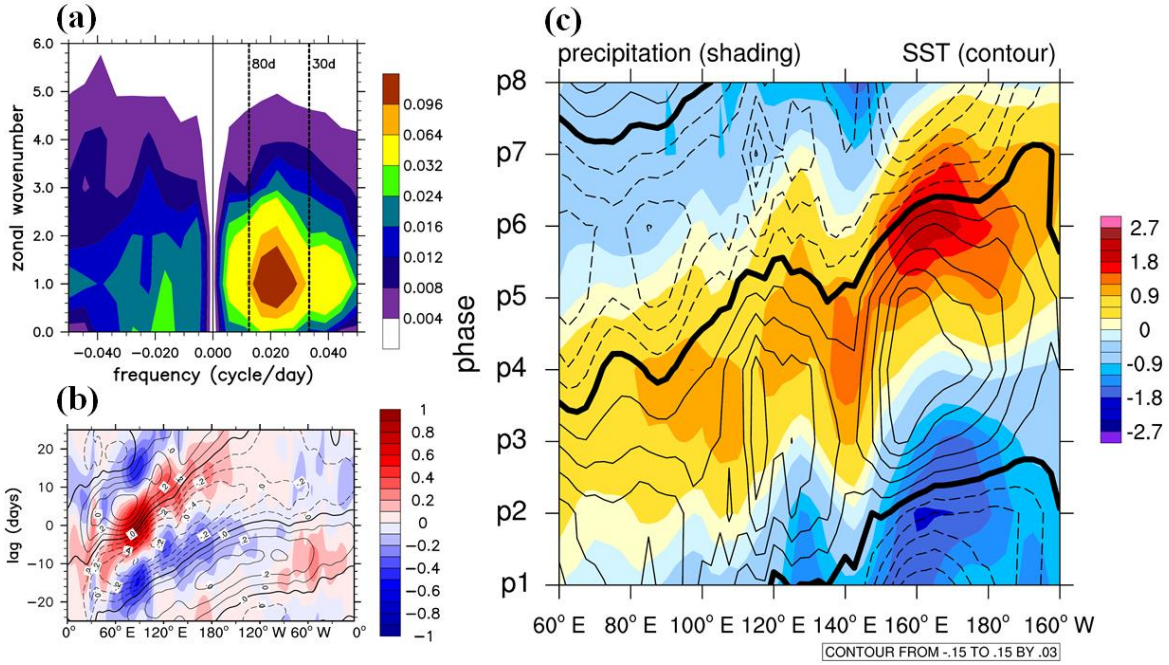

Figure 10. Similar as in Fig. 6 but for the C–30NS–nD.

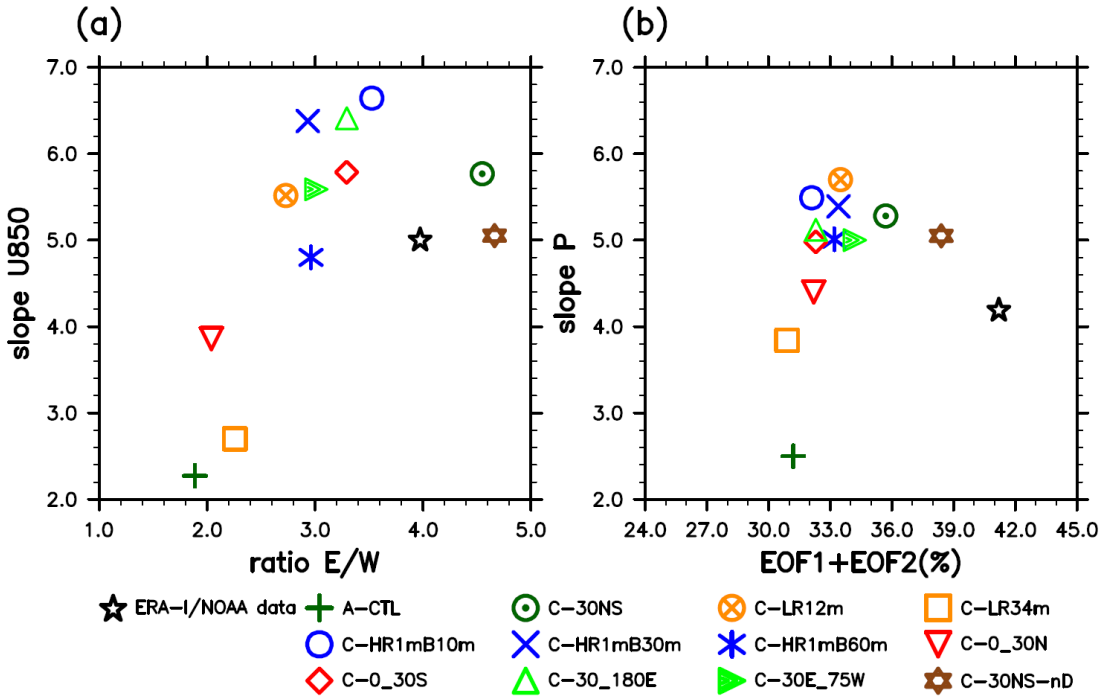

Figure 11. Scattered plots of various MJO indices in the ERA-I/NOAA data and 12 experiments: (a) power ratio of east/west propagating waves of wavenumber 1–3 of 850-hPa zonal winds (X-axis) with a 30–80-day period and eastward propagation speed of U850 anomaly (Y-axis) from the Hovmöller diagram and (b) RMM1 and RMM2 variance and eastward propagation speed of the filtered precipitation anomaly derived from the Hovmöller diagram.

Appendix: 1-D high-resolution TKE ocean model

The 1-D high-resolution turbulence kinetic energy ocean model SIT was used to simulate the diurnal fluctuation of SST and surface energy fluxes. The model was well verified against surface and subsurface observations in the South China Sea (Lan et al., 2010) and the tropical WP (Tu and Tsuang, 2005). Variations in sea water temperature (T), current ($\vec{u}$), and salinity (S) were determined (Gaspar et al., 1990) using the following equations.

$$\frac{\partial T}{\partial t} = (k_h + v_h)\frac{\partial^2 T}{\partial z^2} + \frac{R_{sn}}{\rho_{w0} c_w}\frac{\partial F}{\partial z} \quad (1)$$

$$\frac{\partial \vec{u}}{\partial t} = -f\,\hat{k} \times \vec{u} + (k_m + v_m)\frac{\partial^2 \vec{u}}{\partial z^2} \quad (2)$$

$$\frac{\partial S}{\partial t} = (k_h + v_h)\frac{\partial^2 S}{\partial z^2} \quad (3)$$

where R_{sn} is the net solar radiation at the surface (W m^{-2}), $F(z)$ is the fraction (dimensionless) of R_{sn} that penetrates to the depth z, and k_h and k_m are eddy diffusion coefficients for heat and momentum (m^2 s^{-1}), respectively. The value of k_h within the cool skin layer and that of k_m within the viscous layer were set to zero. Molecular transport is the only mechanism for the vertical diffusion of heat and momentum in the cool skin and viscous layer, respectively (Hasse, 1971; Grassl, 1976; Wu, 1985).The parameters ν_m and ν_h are the molecular diffusion coefficients for momentum and temperature, respectively, ρ_{w0} is the density (kg m^{-3}) of water, and c_w is the specific heat capacity of water at constant pressure (J kg^{-1} K^{-1}). S is salinity (‰), $\vec{u}$ is the current velocity (m s^{-1}), f is the Coriolis parameter (dimensionless), and $\hat{k}$ is the vertical unit vector (m s^{-1}).

Using the numerical solution of the surface layer (T_0), we disregard the time-term of the 2-metre air temperature (T_{2m}), which can be considered the upper boundary of an ocean, as well as the numerical solution of the surface long-wave radiation T_0 term and aerodynamic resistance (r_a).

$$
\begin{aligned}
\frac{\partial T_0}{\partial t} &= \frac{G_0}{\rho_w \cdot c_w \cdot h_e} + \frac{R_{sn}[F(z_0) - F(z_0 - d)]}{\rho_w \cdot c_w \cdot h_e} - \frac{G_{0,1}}{\rho_w \cdot c_w \cdot h_e} \\
&= \frac{R_{ld} - R_{lu} - H - LE}{\rho_w \cdot c_w \cdot h_e} + \frac{R_{sn}[F(z_0) - F(z_0 - d)]}{\rho_w \cdot c_w \cdot h_e} - k_0 \frac{T_0 - T_1}{h_e(z_0 - z_1)} \\
&= \frac{1}{\rho_w \cdot c_w \cdot h_e}[R_{ld} - \varepsilon\sigma T_0^4 - \frac{\rho_a c_a (T_0 - T_{2m})}{r_a} - \frac{\rho_a L_v (q^*(T_0) - q_a)}{r_a}] \\
&+ \frac{R_{sn}[F(z_0) - F(z_0 - d)]}{\rho_w \cdot c_w \cdot h_e} - k_0 \frac{T_0 - T_1}{h_e(z_0 - z_1)}
\end{aligned}
\tag{3}
$$

where G_0 is the net flux of the ocean surface, $G_{0,1}$ is the net flux in the bottom depth of T_0 grid, and K_0 and h_e are eddy diffusion coefficients and the effective thickness of T_0 layer, respectively. c_a is the specific heat capacity of surface air at constant pressure (J kg^{-1} K^{-1}). L_v is the latent heat of evaporation of water q. We use finite difference approximation to divide time-term into j+1 and j.

$$
\begin{aligned}
\frac{T_0^{j+1} - T_0^j}{\Delta t} &= \frac{1}{\rho_w \cdot c_w \cdot h_e}\{R_{ld} - \varepsilon\sigma(T_0^j)^4 - \frac{\rho_a c_a}{r_a}[\beta T_0^{j+1} + (1-\beta)T_0^j - T_{2m}^j] \\
&- \frac{\rho_a L_v (q^*(T_0) - q_a)}{r_a}\} + \frac{R_{sn}[F(z_0) - F(z_0 - d)]}{\rho_w \cdot c_w \cdot h_e} \\
&- \frac{k_0}{h_e(z_0 - z_1)}[(\beta T_0^{j+1} + (1-\beta)T_0^j) - (\beta T_1^{j+1} + (1-\beta)T_1^j)]
\end{aligned}
\tag{4}
$$

$$
\begin{aligned}
&(1 + \frac{\Delta t}{\rho_w \cdot c_w \cdot h_e}\frac{\rho_a c_a}{r_a}\beta + \frac{k_0 \cdot \Delta t}{h_e(z_0 - z_1)}\beta)T_0^{j+1} - \frac{k_0 \cdot \Delta t}{h_e(z_0 - z_1)}\beta T_1^{j+1} \\
&= T_0^j + \frac{\Delta t}{\rho_w \cdot c_w \cdot h_e}[R_{ld} - \frac{\rho_a L_v (q^*(T_0) - q_a)}{r_a}] + \Delta t \frac{R_{sn}[F(z_0) - F(z_0 - d)]}{\rho_w \cdot c_w \cdot h_e} \\
&+ (1-\beta)(\frac{\Delta t}{\rho_w \cdot c_w \cdot h_e} + \frac{\rho_a c_a}{r_a} + \frac{k_0 \cdot \Delta t}{h_e(z_0 - z_1)})T_0^j - \frac{\Delta t}{\rho_w \cdot c_w \cdot h_e}\varepsilon\sigma(T_0^j)^4 \\
&+ \frac{k_0 \cdot \Delta t}{h_e(z_0 - z_1)}(1-\beta)T_1^j \\
&= T_0^j + \frac{\Delta t}{\rho_w \cdot c_w \cdot h_e}[R_{ld} - \frac{\rho_a L_v (q^*(T_0) - q_a)}{r_a} - \varepsilon\sigma(T_0^j)^4] \\
&+ \Delta t \frac{R_{sn}[F(z_0) - F(z_0 - d)]}{\rho_w \cdot c_w \cdot h_e} - (1-\beta)(\frac{\Delta t}{\rho_w \cdot c_w \cdot h_e} + \frac{\rho_a c_a}{r_a} + y_0)T_0^j \\
&- (1-\beta)y_0(T_0^j - T_1^j)
\end{aligned}
\tag{5}
$$

Since the T_1 is next temperature below the T_0, the numerical solution is based on the

1199 average temperature of the h_1 layer, $h_1 = z_0 - 0.5(z_1 + z_2)$. The parameter β controls the

1200 time scheme (i.e., 1 controls a backward time scheme, 0.5 controls a Crank-Nicolson

1201 method, and 0 controls a forward time scheme).

$$\frac{\partial T_1}{\partial t} = \frac{G_0 + G_{1,2}}{\rho_w \cdot c_w \cdot h_1} + \frac{R_{sn}[F(z_0) - F(\frac{z_1 + z_2}{2})]}{\rho_w \cdot c_w \cdot h_1}$$

$$= \frac{h_e}{h_1}\frac{\partial T_0}{\partial t} + k_0 \frac{T_0 - T_1}{h_1(z_0 - z_1)} + \frac{R_{sn}[F(z_0) - F(\frac{z_1 + z_2}{2})]}{\rho_w \cdot c_w \cdot h_1} - k_1 \frac{T_1 - T_2}{h_1(z_1 - z_2)}$$

1202
$$\frac{T_1^{j+1} - T_1^j}{\Delta t} = \frac{h_e}{h_1}\frac{T_0^{j+1} - T_0^j}{\Delta t} + k_0 \frac{[\beta T_0^{j+1} + (1-\beta)T_0^j] - [\beta T_1^{j+1} + (1-\beta)T_1^j]}{h_1(z_0 - z_1)} \quad (6)$$

$$+ \frac{R_{sn}[F(z_0 - d) - F(\frac{z_1 + z_2}{2})]}{\rho_w \cdot c_w \cdot h_1} - \frac{k_1}{h_1(z_1 - z_2)}[(\beta T_1^{j+1} + (1-\beta)T_1^j)$$

$$- (\beta T_2^{j+1} + (1-\beta)T_2^j)]$$

1203 Specifically, the numerical solution of the next T_2 below the T_1 is not affected by the G_0

1204 term, and that of the energy term is mainly affected by the $G_{1,2}$, $G_{2,3}$, and R_{sn} components.

$$\frac{\partial T_2}{\partial t} = \frac{-G_{1,2} + G_{2,3}}{\rho_w \cdot c_w \cdot h_2} + \frac{R_{sn}[F(\frac{z_1 + z_2}{2}) - F(\frac{z_2 + z_3}{2})]}{\rho_w \cdot c_w \cdot h_2}$$

$$= \frac{R_{sn}[F(\frac{z_1 + z_2}{2}) - F(\frac{z_2 + z_3}{2})]}{\rho_w \cdot c_w \cdot h_2} + k_1 \frac{T_1 - T_2}{h_2(z_1 - z_2)} - k_2 \frac{T_2 - T_3}{h_2(z_2 - z_3)}$$

1205
$$\frac{T_2^{j+1} - T_2^j}{\Delta t} = \frac{R_{sn}[F(\frac{z_1 + z_2}{2}) - F(\frac{z_2 + z_3}{2})]}{\rho_w \cdot c_w \cdot h_2} + k_1 \frac{[\beta T_1^{j+1} + (1-\beta)T_1^j] - [\beta T_2^{j+1} + (1-\beta)T_2^j]}{h_2(z_1 - z_2)} \quad (7)$$

$$- k_2 \frac{[\beta T_2^{j+1} + (1-\beta)T_2^j] - [\beta T_3^{j+1} + (1-\beta)T_3^j]}{h_2(z_1 - z_2)}$$

1206 Similarly, the numerical solutions of layers between 3 and 41 are as follows:

1207
$$(-\beta x_k)T_{k-1}^{j+1} + (1 + \beta \cdot x_k + \beta \cdot y_k)T_2^{j+1} - \beta \cdot y_k T_{k+1}^{j+1}$$

$$= T_k^j + \frac{\Delta t \cdot R_{sn}}{\rho_w \cdot c_w \cdot h_k}\{R_{sn}[F(\frac{z_{k-1} + z_k}{2}) - F(\frac{z_k + z_{k+1}}{2})]\} + (1-\beta)[x_k(T_{k-1}^j - T_k^j) \quad (8)$$

$$- y_2(T_k^j - T_{k+1}^j)]$$

where $y_0 = \frac{\Delta t}{h_e}\frac{k_0}{z_0 - z_1}$

$$x_k = \frac{\Delta t}{h_k}\left(\frac{k_{k-1}}{k_{k-1} - k_k}\right) \quad for \quad k = 1, n$$

$$y_k = \frac{\Delta t}{h_k}\left(\frac{k_k}{k_k - k_{k+1}}\right) \quad for \quad k = 1, n$$

$$x_g = \frac{\Delta t \cdot \rho_w \cdot c_w}{\rho_g \cdot c_g \sqrt{\frac{k_g}{w}}}\left(\frac{k_n}{z_n - z_g}\right)$$

Finally, we get a triangular matrix for numerical solutions of 1-D high-resolution turbulence kinetic energy ocean model SIT.

$$\begin{bmatrix} 1+\beta\frac{\Delta t}{\rho_w c_w h_e}\frac{\rho_a c_a}{r_a}+y_0\beta & -\beta y_0 & & & & & \\ -\beta x_1-\frac{h_e}{h_1} & 1+\beta x_1+\beta y_1 & -\beta y_1 & & & & \\ & & -\beta x_k & 1+\beta x_k+\beta y_k & -\beta y_k & & \\ & & & & & -\beta x_g & 1+\beta x_g \end{bmatrix} \begin{bmatrix} T_0^{j+1} \\ T_1^{j+1} \\ T_{k-1}^{j+1} \\ T_k^{j+1} \\ T_{k+1}^{j+1} \\ T_n^{j+1} \\ T_g^{j+1} \end{bmatrix} =$$

$$\begin{bmatrix} T_0^j + \frac{\Delta t \cdot R_{sn}[F(z_0)-F(z_0-d)]}{\rho_w c_w h_e} + \frac{\Delta t}{\rho_w c_w h_e}[R_{ld} - \frac{\rho_a L_v (q^*(T_0^j)-q_a)}{r_a} - \varepsilon\sigma(T_0^j)^4] - (1-\beta)[(\frac{\Delta t}{\rho_w c_w h_e}\frac{\rho_a c_a}{r_a}+y_0)T_0^j + y_0(T_0^j - T_1^j)] \\ T_1^j - \frac{h_e}{h_1}T_0^j + \frac{\Delta t \cdot R_{sn}}{\rho_w c_w h_1}\left[F(z_0-d) - F\left(\frac{z_1+z_2}{2}\right)\right] + (1-\beta)[x_1(T_0^j - T_1^j) - y_1(T_1^j - T_2^j)] \\ T_k^j + \frac{\Delta t \cdot R_{sn}}{\rho_w c_w h_k}\left[F\left(\frac{z_{k-1}+z_k}{2}\right) - F\left(\frac{z_k+z_{k+1}}{2}\right)\right] + (1-\beta)[x_k(T_{k-1}^j - T_k^j) - y_k(T_k^j - T_{k+1}^j)] \\ T_g^j + \frac{\Delta t R_{sn} F(z_g)}{\rho_g c_g \sqrt{\frac{k_g}{\omega}}} + (1-\beta)x_g(T_n^j - T_g^j) \end{bmatrix}$$

The eddy diffusivity for momentum k_m is simulated using an eddy kinetic energy approach based on the Prandtl–Kolmogorov hypothesis as follows:

$$k_m = c_k l_k \sqrt{E} \tag{9}$$

where c_k = 0.1 (Gaspar et al., 1990), l_k is the mixing length (m), and

$E = 0.5\left(u'^2 + v'^2 + w'^2\right)$ is turbulent kinetic energy. The turbulent kinetic energy (E) is determined using a 1-D equation (Mellor and Yamada, 1982) as follows:

$$\frac{\partial E}{\partial t} = \frac{\partial}{\partial z} k_m \frac{\partial E}{\partial z} + k_m \left(\frac{\partial \vec{u}}{\partial z}\right)^2 + k_h \frac{g}{\rho_w} \frac{\partial \rho_w}{\partial z} - c_\varepsilon \frac{E^{3/2}}{l_\varepsilon} \quad (10)$$

where $c_\varepsilon = 0.7$ (Gaspar et al., 1990), g is the gravity (m s^{-2}), ρ_w is the density of water (kg m^{-3}), and l_ε is the characteristic dissipation length (m). The mixing length (l_k) and dissipation length (l_ε) were determined following the approach reported by Gaspar et al. (1990). This approach is valid for determining the eddy diffusivity of both the ocean mixed layer and surface layer.

In the SIT model setting, the specific heat of sea water is a constant (4186.84 J kg^{-1} K^{-1}), and the Prandtl number in water is defined as the ratio of momentum diffusivity to thermal diffusivity, which is a dimensionless number set as a constant (1.0). The kinematic viscosity is a constant (1.14×10^{-6} m^2 s^{-1}; Paulson and Simpson, 1981), and the downward solar radiative flux into water with nine wavelength bands was determined following the approach reported by Paulson and Simpson (1981). The minimum turbulent kinetic energy is set to 10^{-6} m^2 s^{-2}, and the zero displacement is set to 0.03 m.

The resolution in the upper 10.5 m is considerably fine to capture the upper-ocean warm layer, and the thickness of the first layer below sea surface is 0.05 mm to reproduce the ocean surface cool skin. The vertical grid within 107.8 m in C–30NS, C–LR12m and C–LR34m as Fig. A1. Besides SST cool skin layer, C–LR12m and C–LR34m have a first layer with grid center of -11.5 m and -33.9 m, respectively. In lowest boundary experiment, the total vertically-gridded layers in C–HR1mB10m, C–HR1mB30m and C–HR1mB60m are showed as Fig. A2.

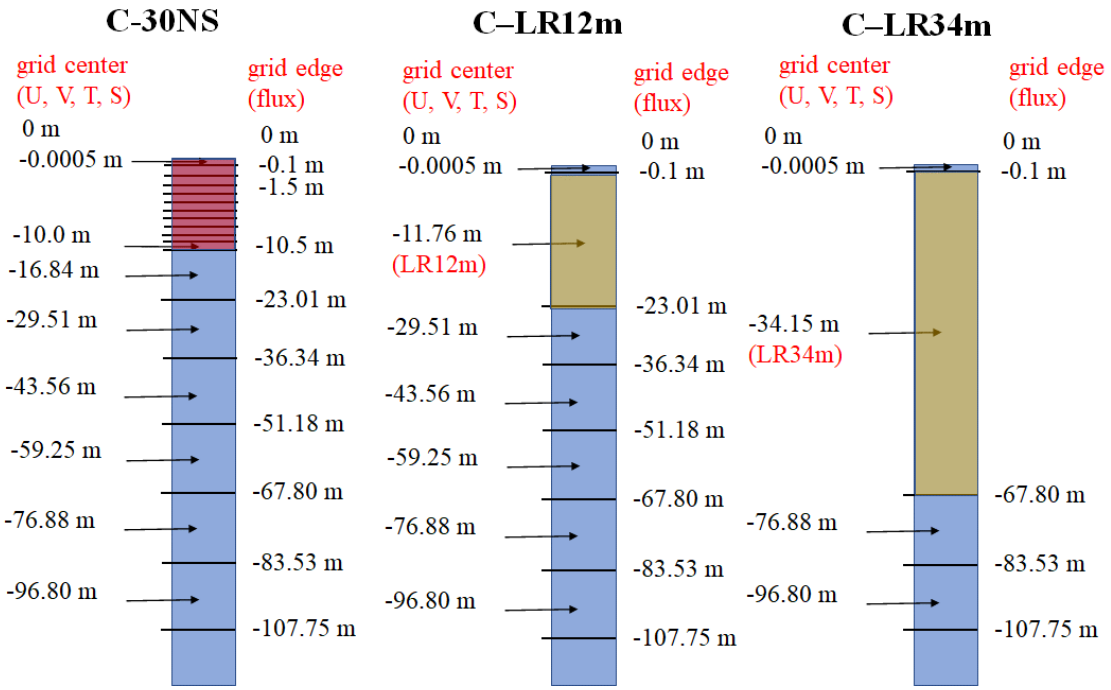

Figure A1. Diagram showing the vertical grid within 107.8 m in C–30NS, C–LR12m and C–LR34m, the model is as thick as 107.8 meters and with several layers between surface and model bottom. C–LR12m (31 vertical layers) and C–LR34m (28 vertical layers) have a first layer with grid center of 12 m and 34 m, respectively, but have the same vertical discretization as in the control experiment (C–30NS, 41 vertical layers) below the first layer.

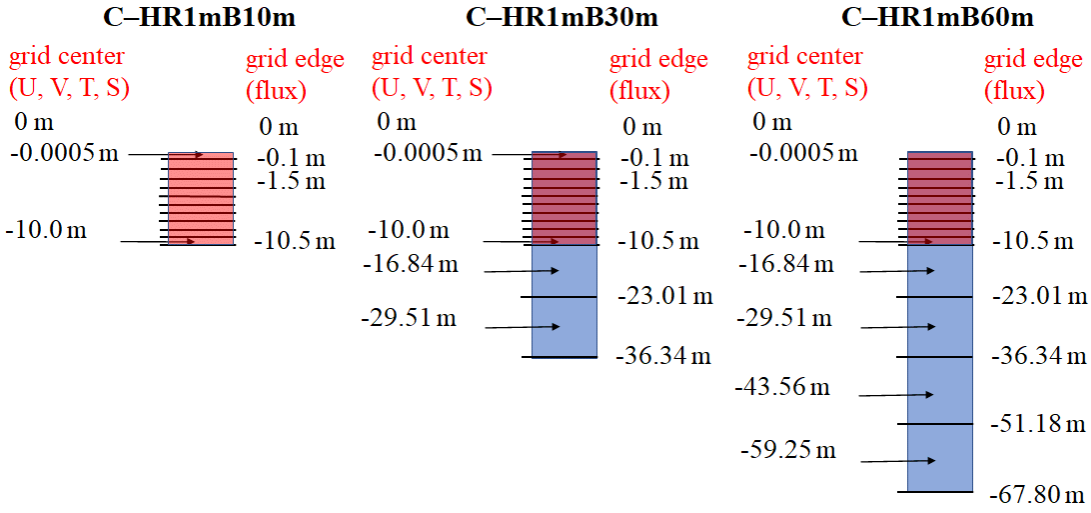

Figure A2. Diagrams showing the vertical grids in C–HR1mB10m, C–HR1mB30m and C–HR1mB60m. The model bottoms are 10, 30, and 60 m, respectively, unless the seabed is shallower than the above depth.

Reference

Gaspar, P., Gregoris, Y., and Lefevre, J.-M.: A simple eddy kinetic energy model for simulations of the oceanic vertical mixing: tests at station papa and long-term upper ocean study site, J. Geophys. Res. -Oceans, 95, 16179–16193, https://doi.org/10.1029/JC095iC09p16179, 1990.

Grassl, H.: The dependence of the measured cool skin of the ocean on wind stress and total heat flux, Bounday-Layer Meteorol., 10, 465-474, https://doi.org/10.1007/BF00225865, 1976.

Hasse, L.: The sea surface temperature deviation and the heat flow at the sea–air interface, Bounday-Layer Meteorol., 1, 368-379, https://doi.org/10.1007/BF02186037, 1971.

Lan, Y.-Y., Tsuang, B.-J., Tu, C.-Y., Wu, T.-Y., Chen, Y.-L., and Hsieh, C.-I.: Observation and Simulation of Meteorology and Surface Energy Components over the South China Sea in Summers of 2004 and 2006, Terr. Atmos. Ocean. Sci., 21, 325–342, https://doi.org/ 10.3319/TAO.2009.04.07.01(A), 2010.

Mellor, G. L., and Yamada, T.: Development of a turbulence closure model for geophysical fluid problems, Rev. Geophys., 20, 851-875, https://doi.org/10.1029/RG020i004p00851, 1982.

Paulson, C. A. and Simpson, J. J.: The temperature difference across the cool skin of the ocean, J. Geophys. Res., 86, 11044-11054, https://doi.org/10.1029/JC086iC11p11044, 1981.

Tu, C.-Y., and Tsuang, B.-J.: Cool-skin simulation by a one-column ocean model, Geophys. Res. Lett., 32, L22602, https://doi.org/10.1029/2005GL024252, 2005.

Wu, J.: On the cool skin of the ocean, Bounday-Layer Meteorol., 31, 203-207, https://doi.org/10.1007/BF00121179, 1985.